Marine Stratocumulus Convection. Part I: Governing Equations and Horizontally Homogeneous Solutions

WAYNE H. SCHUBERT, JOSEPH S. WAKEFIELD, ELLEN J. STEINER AND STEPHEN K. COX

Department of Atmospheric Science, Colorado State University, Fort Collins 80523

(Manuscript received 29 July 1977, in final form 22 January 1979)

ABSTRACT

A coupled, convective-radiative, boundary-layer model of marine stratocumulus clouds is presented. The model, which is a slight generalization of the cloud-topped, mixed-layer model of Lilly (1968), has as dependent variables the cloud-top height, cloud-base height, mixed-layer moist static energy and total water content, the turbulent fluxes of moist static energy and total water, the cloud-top jumps of moist static energy and total water, the cloud-top temperature, and the net radiative flux divergence at cloud top and in the mixed layer.

Under horizontally homogeneous steady-state conditions the governing equations reduce to a system of algebraic equations which is easily solved. This system has been solved for sea surface temperatures between 13 and 18°C and large-scale divergences between 1×10^{-6} and 6×10^{-6} s^{-1}. These calculations have been performed for the case when all the radiative cooling is confined to the cloud-top jump condition and for the case when some of the cooling is allowed to extend into the mixed layer. The results show that the general pattern of mixed-layer response to sea surface temperature and large-scale divergence is not highly sensitive to the radiation partition. The results also show that the thermodynamic properties of the mixed layer and the surface fluxes of moist static energy and water vapor are sensitive to sea surface temperature but not to large-scale divergence. However, the mixed-layer depth is sensitive to large-scale divergence. Roughly speaking, the depth is inversely proportional to divergence so that halving the divergence approximately doubles the depth of the layer, which means that the cloud top seeks a certain subsidence (entrainment) rate. The turbulent fluxes of heat, water vapor and liquid water are discontinuous at cloud base. These discontinuities are interpreted in terms of convective parcel paths.

1. Introduction

In tropical and subtropical latitudes there exists a subtype of dry climate called the cool coastal dry climate, which is classified in Köppen symbols as Bn, with the n signifying frequent fog (Nebel in German). Bn deserts are typically characterized by intense aridity, small annual and diurnal temperature ranges, and high frequences of fog and low stratus. The geographical regions of the five principle Bn climates, their desert names, and the bordering ocean currents are listed in Table 1.

Satellite-derived mean relative cloud cover data indicate that the Bn deserts lie primarily on the borders of extensive stratocumulus regimes which occupy the strong subsidence regions to the east of the subtropical oceanic high pressure cells.[1] The persistent low-level stratocumulus clouds occupy large portions of the eastern Pacific and eastern Atlantic Oceans but only a small portion of the western Indian Ocean. These areas of marine stratocumulus convection are most extensive in the Northern Hemisphere summer, when the upward motion in the ITCZ and the downward motion in the subtropical highs is strongest. We now examine each of these areas in some detail.

a. Coastal Oregon, California and Mexico

In Table 2, we present precipitation data for coastal Oregon, California and Mexico between about 46 and 15°N. The most arid station in an annual sense is Ensenada with 161 mm. North of Ensenada all stations show little summertime precipitation. While a summertime minimum in precipitation occurs between Astoria and Ensenada, a summertime maximum occurs between La Paz and Tapachula. This is consistent with the fact that the area east and south of La Paz is under the influence of summertime tropical disturbances and, in fact, is an area of frequent tropical storms and hurricanes—on the average 11 in the July–September period (Gunther, 1977). If these tropical cyclones move northwest toward the stratocumulus regime, they usually dissipate rapidly as they encounter lower sea surface temperatures.

An example of the eastern North Pacific stratocumulus regime is shown in Figs. 1 and 2. The temperature, moisture and wind profiles shown in Fig. 2

[1] Coastal northeastern Africa is the exception.

0022-4928/79/071286-22$09.50
© 1979 American Meteorological Society

TABLE 1. The five principle cool coastal dry climates, their accompanying desert names and their bordering cool ocean currents.

Region	Desert	Ocean current
Coastal California and Mexico	Sonoran	California
Coastal Ecuador, Peru and Chile	Peru and Atacama	Peru or Humboldt
Coastal northwestern Africa	Sahara	Canaries
Coastal southwestern Africa	Namib	Benguela
Coastal northeastern Africa	Somali	Somali

are from an NCAR Electra[2] sounding at 37.8°N, 125.0°W and within 1 h of the satellite image. The sounding shows the structure of the mixed layer and the inversion layer quite well. The subcloud layer is dry adiabatic, the cloud layer is moist adiabatic, and the inversion layer is extremely stable with a potential temperature increase of about 11 K in 10 mb. The sea surface temperature is very near the surface air temperature. Radiosonde observations tend to considerably smooth such a structure.

b. Coastal Ecuador, Peru and Chile

Precipitation data for coastal Ecuador, Peru and Chile are shown in Table 3. The table shows that aridity exists between about 5 and 30°S and is particularly intense between 18 and 24°S. Even Guayaquil, which is very near the equator, experiences very little precipitation during the second half of the year. The Peruvian-Chilean desert is the most arid and the latitudinally most extensive of the five primary Bn deserts. An annual rainfall of under 120 mm is maintained along a thin coastal strip about 25° latitude in length. Two unique features of this region are the presence of high mountains close to the coast and the existence of a coastline which bends continuously into rather than away from the atmospheric and oceanic circulations.

It should be pointed out that the precipitation data for northern Peru has high interannual variability. Normally in December the southeast trades and the coastal upwelling weaken and warm water appears between Guayaquil and El Alto. This is associated with increased rainfall in the first few months of the year. During occasional major El Niño events the warm water appears considerably farther south causing torrential rains at normally arid stations. For example, during March of the 1972 El Niño event, El Alto recorded 587 mm of precipitation.

[2] These data are discussed more fully in Wakefield and Schubert (1976).

TABLE 2. Mean precipitation (mm) for stations along coastal Oregon, California and Mexico. Data for this and the following four tables was taken from U. S. Dept. of Commerce (1959, 1968).

Station	Latitude (°N)	JFM	AMJ	JAS	OND	Year
Astoria	46.2	714	270	140	733	1857
North Bend	43.4	667	211	68	624	1570
Eureka	40.8	497	141	27	376	1041
San Francisco	37.6	264	59	9	164	496
Los Angeles	33.9	201	50	2	75	328
Ensenada	31.9	75	28	4	54	161
La Paz	24.2	18	12	98	43	171
Mazatlan	23.2	29	32	611	104	776
Manzanillo	19.1	26	177	754	194	1151
Acapulco	16.8	16	319	936	248	1519
Tapachula	14.9	27	803	1189	498	2517

c. Coastal northwestern Africa

Table 4 gives precipitation data for coastal northwestern Africa, the Canary Islands and the Cape Verde Islands. The most arid stations lie between 28 and 21°N. This includes the coast of Spanish Sahara, which is known for active upwelling (LaViolette, 1974). A typical example (0900 GMT 12 August 1974) of a GATE SMS visible image is shown in Fig. 3. The large stratocumulus area off the coast of northwestern Africa extends southward almost to the GATE array. The stratocumulus area off the coast of southwestern Africa is seen to extend northward almost to the equator. Fig. 3 also shows the mean July–September precipitation for coastal and island stations and for GATE A/B- and B-scale ships. It is apparent that the low-level stratocumulus clouds are associated with low precipitation amounts.

d. Coastal southwestern Africa

Precipitation data for the coast of southwestern Africa are shown in Table 5. Between 15 and 30°S the mean annual precipitation is less than about 60 mm. Between 22 and 27°S the aridity is particularly intense with mean annual precipitation around 15 mm. Although the mean annual precipitation increases rapidly north of 15°S, Table 5 reveals that aridity extends far equatorward during July–September.

e. Coastal northeastern Africa

The region of coastal northeastern Africa and the western Arabian Sea exhibits extreme seasonal differences. In winter northeasterly flow dominates, while in summer both the oceanic and atmospheric circulations are reversed. The summertime oceanic

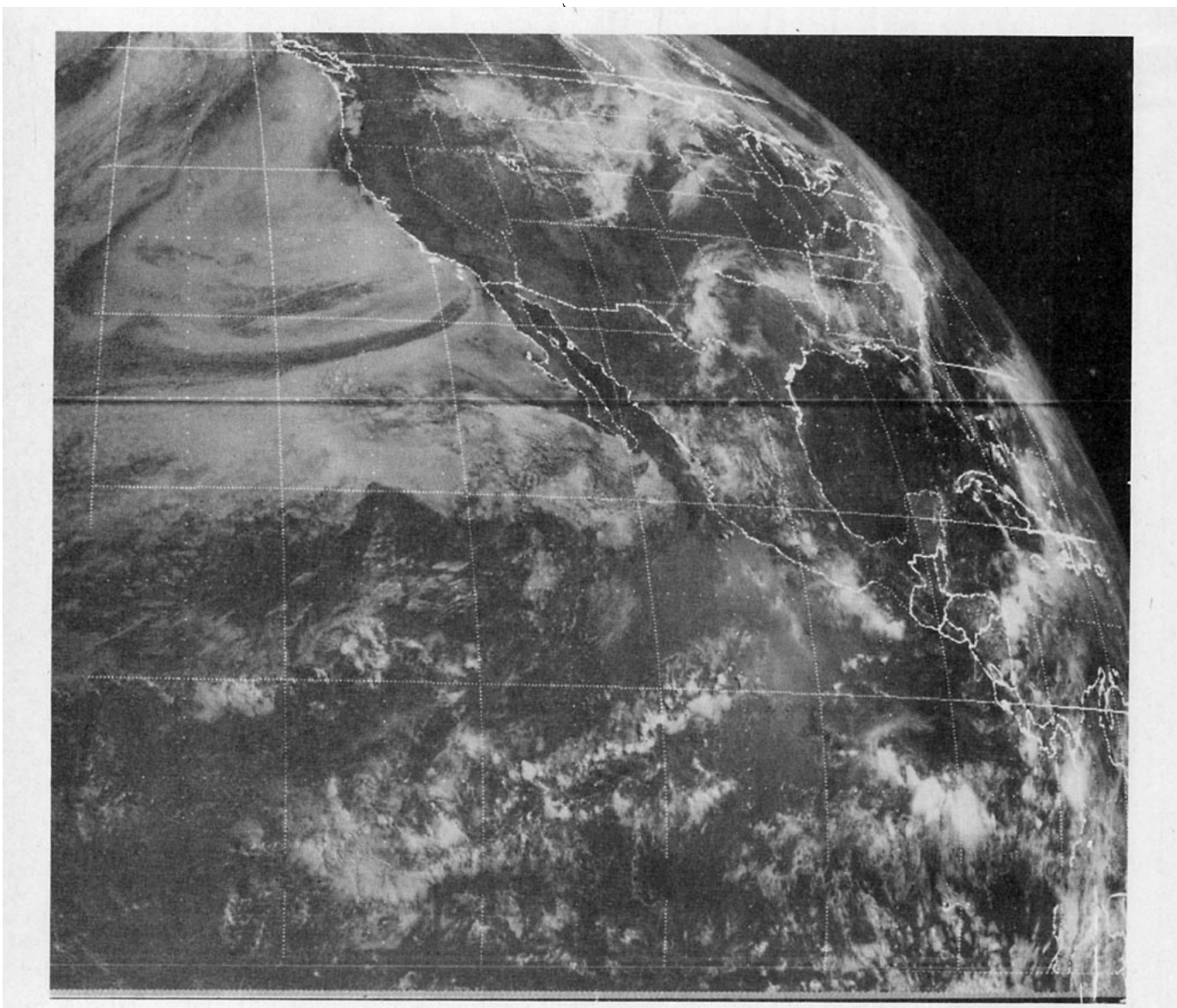

FIG. 1. SMS/GOES visible image for 1615 GMT 17 June 1976.

situation is characterized by intense upwelling (Warren *et al.*, 1966; Leetmaa, 1972), while the summertime atmospheric situation is characterized by strong divergent southwesterly flow [see Fig. 4, adapted from Ramage (1966), and Flohn *et al.*, (1968)]. According to Trewartha (1961) there is a high incidence of fog along the Somalia coast in the summer months, while fog is rare in December and January. Precipitation data for this region are given in Table 6.

f. Other stratocumulus regions

Although we have discussed only the five primary Bn deserts and their associated cloud systems, we do not mean to imply that stratocumulus clouds are limited to these areas. For example, stratocumulus often occur near the coast of Australia (Paltridge, 1974; Platt, 1976), and during wintertime cold air outbreaks over the Kuroshio Current (e.g., Ninomiya, 1975; Nitta, 1976; Lenschow and Agee, 1976), the Gulf Stream and the Great Lakes (Lenschow, 1973). In Part II of this paper (Schubert *et al.*, 1979), we present an example of a cold air outbreak over the Kuroshio Current during AMTEX '75.

g. Outline

In the remainder of this paper, we shall present a coupled, convective-radiative, boundary-layer model of marine stratocumulus convection, after which we shall study the horizontally homogeneous, steady-state solutions of the model. Horizontally inhomogeneous solutions are discussed in Part II.

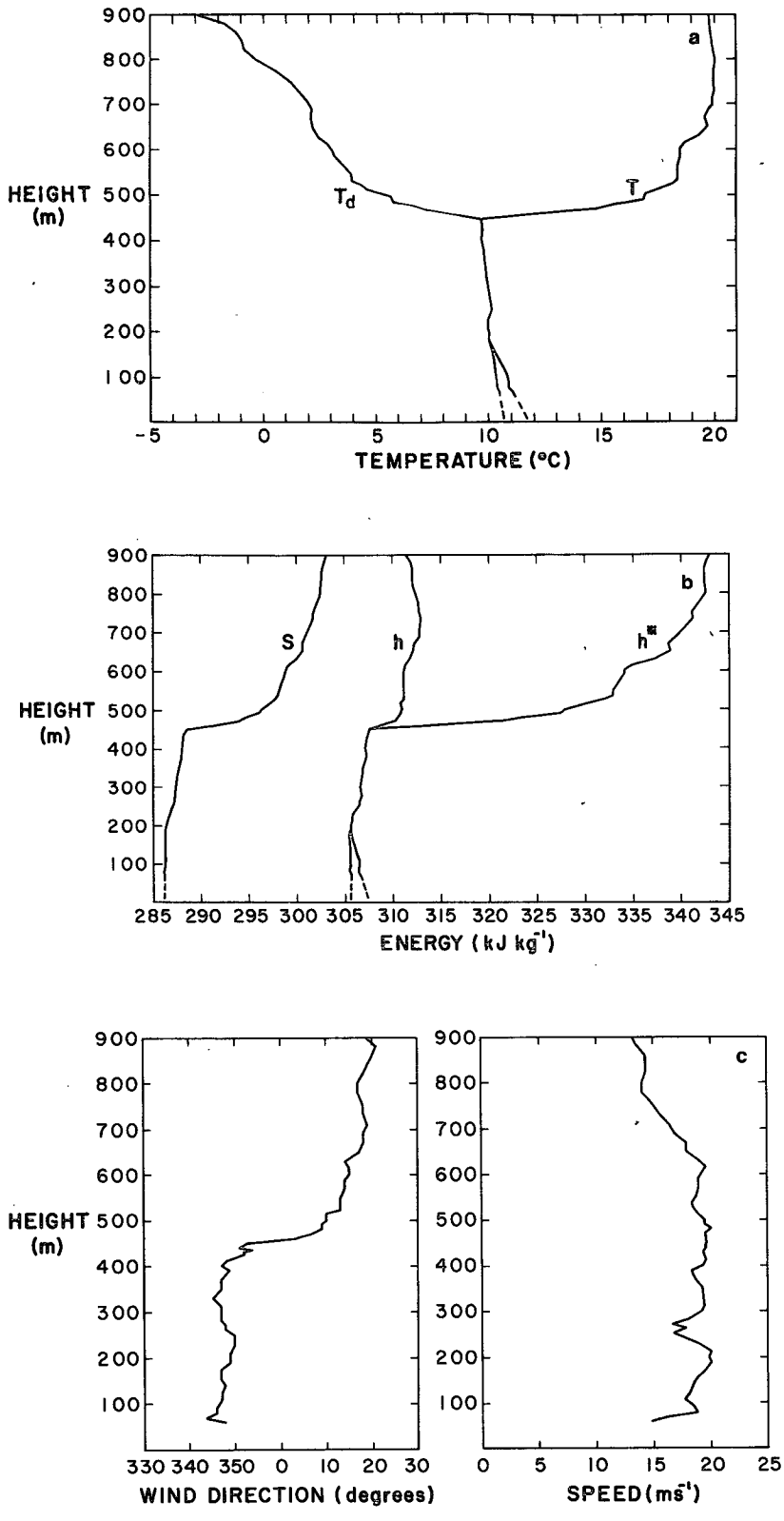

FIG. 2. Temperature, moisture and wind data from an NCAR Electra sounding at 37.8°N, 125.0°W and between 1522 and 1526 GMT: (a) temperature and dew point; (b) dry static energy, moist static energy and saturation static energy; (c) wind direction and speed. Dashed lines below 50 m are extrapolations.

TABLE 3. Precipitation (mm) for stations along coastal Ecuador, Peru and Chile.

Station	Latitude (°S)	JFM	AMJ	JAS	OND	Year
Guayaquil	2.2	699	286	12	26	1023
El Alto	4.3	26	13	1	1	41
Lima	12.1	2	4	11	4	21
Arica	18.5	T	T	T	T	1
Antofagasta	23.5	0	0	T	0	T
Coquimbo	29.9	3	47	41	4	105
Valparaiso	33.0	5	195	141	8	349
Punta Galera	40.0	295	948	1052	282	2577

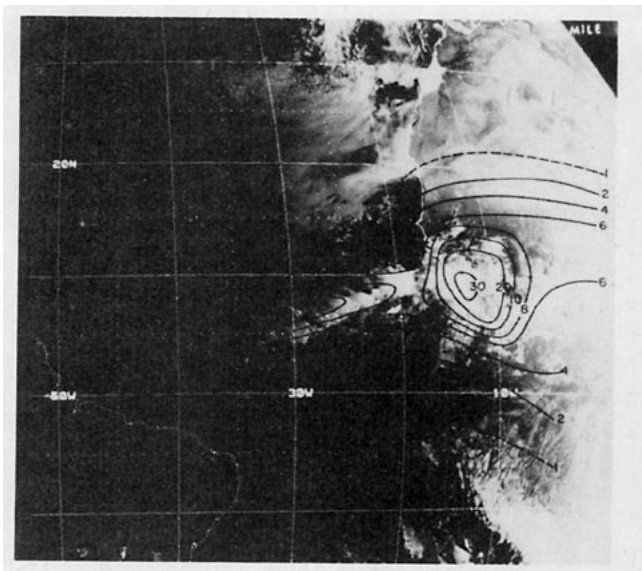

FIG. 3. Typical (0900 GMT, 12 August 1974) SMS visible image taken during GATE. The image shows that stratocumulus area off the coast of northwestern Africa, the northern extent of the stratocumulus area off the coast of southwestern Africa, and a region of disturbed conditions between. Also shown is July–September mean precipitation (mm day^{-1}) for coastal and island stations and for GATE ships.

The coupled, convective-radiative, boundary-layer model presented here is a slight generalization of Lilly's (1968) model. Some aspects of Lilly's model have been studied by Arakawa (1975), Schubert (1976), Deardorff (1976), Randall (1976, 1979a,b), Kraus and Schaller (1978a,b), Kahn and Businger (1979) and Lilly and Schubert (1979). However, there is still great need for systematic study of the horizontally homogeneous and horizontally inhomogeneous solutions to this model. It is hoped that the present study will help remedy this need.

Since the publication of Lilly's paper in 1968, the equations of his model, with some exceptions, have been generally accepted as an elegantly simple description of marine stratocumulus convection. The exceptions center around the relationship between radiative and convective fluxes and entrainment at the top of the mixed layer. Lilly assumed that the radiative cooling was confined to the cloud-top jump condition so that radiation did not appear in the mixed-layer heat budget. Deardorff (1976) and Kahn and Businger (1979) have questioned this assumption. Deardorff has suggested that only some of the radiative cooling should appear in the cloud-top jump condition, while Kahn and Businger have suggested that none should. In an effort to clear up this point, Lilly and Schubert (1979) have studied the effect of internal radiative cooling in a dry "cloud" model. Their conclusion is that for radiation extinction lengths greater than 10–20 m the effect of internal cooling can be important. The present study should at least partially resolve the radiation question for the wet cloud case since we have allowed for radiative cooling both in the cloud-top jump condition and in the mixed-layer heat budget. Lilly (1968) also attempted to find bounds on the entrainment and was led to his maximum and minimum entrainment assumptions. His maximum condition has been generally accepted, but questions concerning his minimum condition have arisen. In particular, Deardorff (1976) has claimed that Lilly's minimum condition needs complete revision. This has led Deardorff to introduce a model with a more complicated vertical

TABLE 4. Precipitation (mm) for stations along coastal northwestern Africa.

Station	Latitude (°N)	JFM	AMJ	JAS	OND	Year
Rabat	34.0	196	79	14	218	507
Safi	32.3	130	39	7	155	331
Sidi Ifni	29.4	63	14	4	69	149
Fuerteventura	28.5	46	6	7	59	118
Tarfaia	27.9	18	6	12	25	61
Villa Cisneros	23.7	6	T	12	15	33
Port Etienne	20.9	7	1	14	14	36
Nouakchott	18.1	3	2	135	32	172
Mindelo	16.9	10	T	72	94	176
Praia	14.9	6	0	133	131	270

TABLE 5. Precipitation (mm) for stations along coastal southwestern Africa.

Station	Latitude (°S)	JFM	AMJ	JAS	OND	Year
Pointe Noire	4.8	595	295	16	444	1350
Banana	6.0	329	179	7	232	747
Luanda	8.8	148	145	3	59	355
Benguela	12.6	155	83	2	58	298
Mocamedes	15.2	27	11	0	5	43
Walvis Bay	23.0	7	3	0	2	12
Luderitz	26.6	5	6	5	1	17
Port Nolloth	29.2	9	22	22	8	61
Cape Town	33.9	49	246	238	82	615

structure, one which has a "double-jump" vertical flux profile. In the present study we have used a weighted average of Lilly's maximum and minimum entrainment conditions. It would be useful to compare the solutions obtained in the present paper and in Part II with the solutions of Deardorff's model. However, solutions analogous to those obtained here are not yet available for Deardorff's model.

Before presenting our slightly generalized version of Lilly's cloud-topped mixed-layer model, we shall find it useful to illustrate our entrainment assumption through the use of the dry model. This is done in Section 2. The cloud-topped mixed-layer model is presented in Section 3. The horizontally homogeneous solutions and their physical interpretation are given in Section 4.

2. Governing equations and solutions for a dry "cloud" layer

We consider first the simplified dry "cloud" layer studied by Lilly (1968). If z_B denotes the depth of the boundary layer and $\overline{w's'}$ the turbulent flux of dry static energy $s = c_pT + gz$, the maximum entrainment assumption of Lilly is

$$\int_0^{z_B} \overline{w's'}dz = 0 \quad \text{but} \quad \overline{w's'} \neq 0 \quad \text{somewhere,} \tag{2.1}$$

while his minimum entrainment assumption is

$$(\overline{w's'})_{\min} = 0 \quad \text{but} \quad \int_0^{z_B} \overline{w's'}dz > 0. \tag{2.2}$$

Lilly's interpretation of the maximum entrainment assumption is that the dissipation and transport terms in the vertically integrated, turbulent kinetic energy equation are negligibly small compared to the opposing positive and negative contributions to the energy conversion term. His interpretation of the minimum entrainment assumption is that the dissipation is so strong that a region of negative heat flux cannot be supported. The entrainment assumption we shall use is simply a weighted average of these two,[3] i.e.,

$$\frac{k}{z_B}\int_0^{z_B} \overline{w's'}dz + \tfrac{1}{2}(1-k)(\overline{w's'})_{\min} = 0, \tag{2.3}$$

where k is a constant such that $0 \leq k \leq 1$. Note that $(\overline{w's'})_{\min} \leq 0$, since otherwise both terms in (2.3) would be positive and the equality would be impossible to satisfy. If we perform the integration in (2.3), we obtain

$$k[(\overline{w's'})_B + (\overline{w's'})_S] + (1-k)(\overline{w's'})_{\min} = 0, \tag{2.4}$$

since $\overline{w's'}$ is linear with height. Here $(\overline{w's'})_S$ is the surface flux, $(\overline{w's'})_B$ the flux just below z_B, and $(\overline{w's'})_{\min}$ the smaller of these two fluxes.

The total radiative flux difference across the inversion layer and the mixed layer[4] is $F_+ - F_S$, which we assume in this section is externally specified. If we define μ such that it represents the fractional flux divergence in the mixed layer, we may partition the total as follows:

$$F_B - F_S = \mu(F_+ - F_S), \tag{2.5a}$$

$$F_+ - F_B = (1-\mu)(F_+ - F_S). \tag{2.5b}$$

We now summarize the equations of our somewhat generalized version of Lilly's dry "cloud" model, which is a closed system of equations in the following unknowns: mixed layer dry static energy s_M, boundary-layer depth z_B, and dry static energy fluxes $(\overline{w's'})_S$ and $(\overline{w's'})_B$. The equations are

$$(\overline{w's'})_S = C_T V[s_S - s_M], \tag{2.6}$$

$$\left.\begin{aligned} (\overline{w's'})_B &= -k(\overline{w's'})_S \quad \text{if } (\overline{w's'})_S > 0 \\ k(\overline{w's'})_B &= -(\overline{w's'})_S \quad \text{if } (\overline{w's'})_S < 0 \end{aligned}\right\}, \tag{2.7a, 2.7b}$$

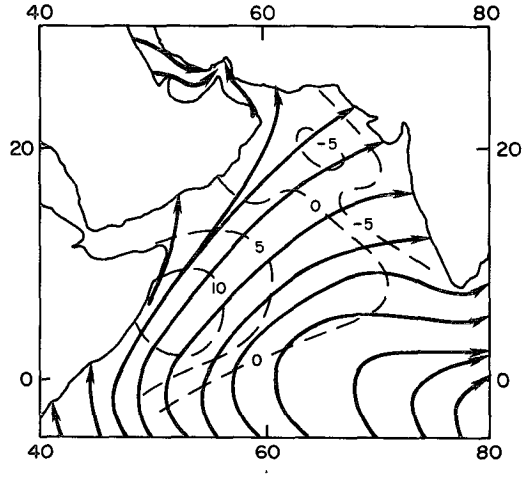

FIG. 4. Mean July–August resultant surface winds and divergence (dashed lines) over Arabian Sea. Isopleths of divergence are labeled in units of 10^{-6} s^{-1}. Adapted from Ramage (1966) and Flohn *et al.* (1968).

TABLE 6. Precipitation (mm) for stations along coastal northeastern Africa.

Station	Latitude	JFM	AMJ	JAS	OND	Year
Socotra	12.4°N	16	33	3	142	194
Bosaso	11.3°N	0	T	0	11	11
Obbia	5.3°N	21	53	3	88	165
Mogadisho	2.0°N	12	238	96	76	422
Kismayu	0.4°S	T	188	79	21	288
Lamu	2.3°S	27	655	140	102	924

[3] The factor ½ in the second term of (2.3) is somewhat arbitrary, but its omission simply results in a revised interpretation of the parameter k.

[4] For a function which is discontinuous across z_B we use the subscript + for the value just above z_B and the subscript B for the value just below z_B. The subscript S is for the surface value.

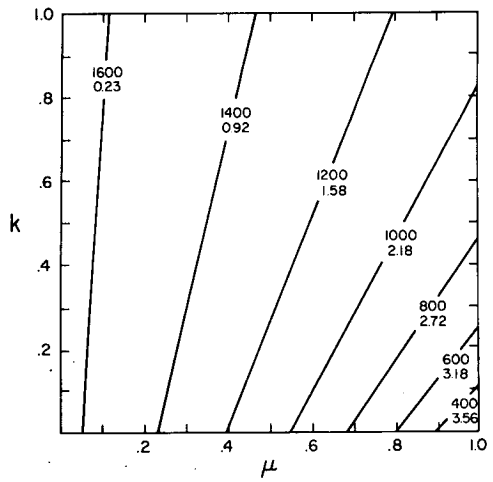

FIG. 5. Isopleths of boundary-layer depth and sea minus air temperature difference in the k-μ domain. The top label is boundary-layer depth (m), the bottom label sea-air temperature difference (°C).

$$\frac{ds_M}{dt} = \frac{(\overline{w's'})_S - (\overline{w's'})_B - \mu(F_+ - F_S)}{z_B}, \quad (2.8)$$

$$\frac{dz_B}{dt} = -Dz_B + \frac{(1-\mu)(F_+ - F_S) - (\overline{w's'})_B}{s_+ - s_M}, \quad (2.9)$$

where C_T is the transfer coefficient, V the surface wind speed, s_S the dry static energy of the surface, D the large-scale divergence, and s_+ the dry static energy of the nonturbulent air just above cloud top. Eq. (2.7) is simply another form of (2.4). Although we have derived (2.7) from the assumption (2.3), it can also be derived from the assumption (see Lilly and Schubert, 1979)

$$\int_{\overline{w's'}<0 \text{ domain}} \overline{w's'}dz = -k^2 \int_{\overline{w's'}>0 \text{ domain}} \overline{w's'}dz, \quad (2.10)$$

which is simply a statement that the ratio of the negative contribution to the energy conversion term to the positive contribution is $-k^2$. The numerical integration of the system (2.6)–(2.9) proceeds in the order given if initial conditions on s_M and z_B are specified.

Before examining the transient solutions of this system, it will be instructive to look at the steady-state solutions. Assuming that $(\overline{w's'})_S > 0$, so that (2.7a) is chosen, the steady-state solution of the system (2.6)–(2.9) can be written

$$\frac{Dz_B}{C_T V} = \frac{1 + k - \mu}{\dfrac{(1+k)C_T V(s_+ - s_S)}{F_+ - F_S} + \mu}, \quad (2.11)$$

$$s_S - s_M = \frac{\mu(F_+ - F_S)}{(1+k)C_T V}. \quad (2.12)$$

Eq. (2.11) must be regarded as an implicit relation for z_B since s_+ depends on z_B. Fig. 5 shows, in the $k - \mu$ domain, isopleths of the steady-state values of boundary-layer depth and sea–air temperature difference, as calculated from (2.11) and (2.12) using the following specified parameters:

$$\left.\begin{aligned} C_T V &= 0.015 \text{ m s}^{-1}, \quad & s_S &= 286.28\ kJ\ \text{kg}^{-1}, \quad & D &= 5.5 \times 10^{-6}\ \text{s}^{-1} \\ F_+ - F_S &= 60\ \text{m}^3\ \text{s}^{-3}, \quad & s_+ &= 283.27\ kJ\ \text{kg}^{-1} + 5.76\ kJ\ \text{kg}^{-1}\ \text{km}^{-1}\ z_B \end{aligned}\right\}.$$

The original Lilly model ($\mu = 0$) produces a deep layer (1662 m) with zero sea–air temperature difference. Note that in the $\mu = 0$ case the steady-state solutions are independent of k. As μ increases the layer becomes shallower and more convective.

Lilly and Schubert (1979), exploring the argument of Deardorff (1976) and Kahn and Businger (1979), have presented steady-state solutions to a dry "cloud" model in which the radiative flux is continuous across cloud top and exponential in the mixed layer. Their radiation extinction length λ is then analogous to our partition parameter μ. Our solutions in the $k - \mu$ domain show the same qualitative features as Lilly and Schubert's solutions in the $k - \lambda$ domain.

Two examples of transient solutions of the system (2.6)–(2.9) are shown in Fig. 6. The computations were made with the same specified parameters as above, with $k = \mu = 0.2$, and with an initial z_B of 700 m. The solid curves are for an initial s_M of 286.50 kJ kg^{-1} (surface air 0.22°C warmer than the sea) while the dashed curves are for an initial s_M of 284.74 kJ kg^{-1} (surface air 1.54°C colder than the sea). Both examples approach the steady-state solution given in Fig. 5 (i.e., z_B = 1476 m and $T_{\text{sea}} - T_{\text{air}}$ = 0.66°C). An interesting feature of Fig. 6 is that the example with smaller surface flux grows more rapidly—a result of the fact that Δs is smaller for this case.

The results of the dry cloud model are primarily of academic interest since water substance cannot be neglected in any realistic stratocumulus model. However, the dry cloud model does illustrate the use of our entrainment assumption and the effect of partitioning the radiative cooling between the jump condition and the mixed layer heat budget equation. In this sense the dry model serves as a

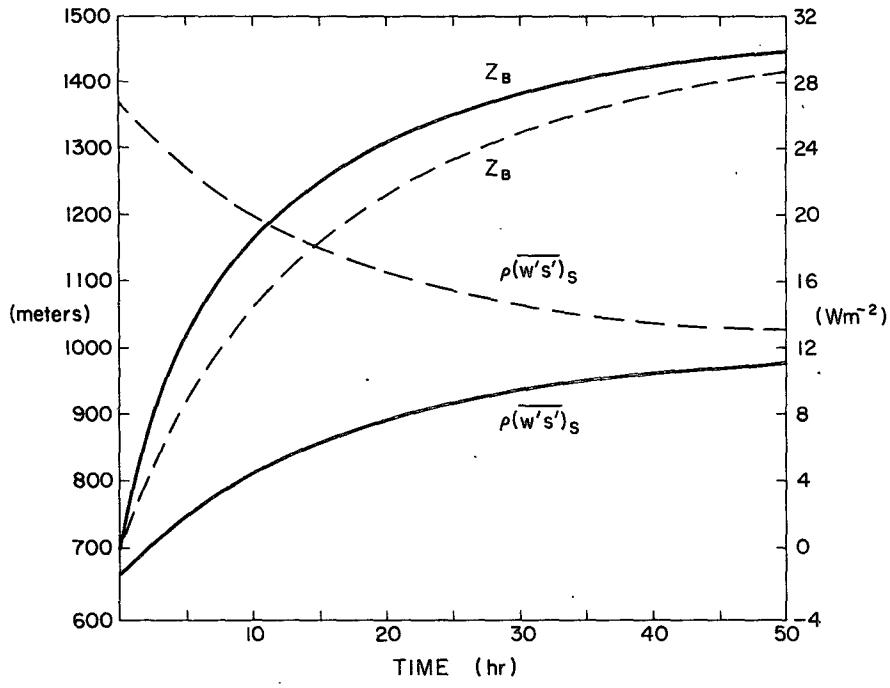

FIG. 6. Two examples of the time variation of z_B and $\rho(\overline{w's'})_S$ for $k = \mu = 0.2$. Solid curves are for an initial condition in which the surface air is 0.22°C warmer than the sea, dashed curves for surface air initially 1.54°C colder than the sea.

basis for understanding the more complicated cloud-topped mixed-layer model of the next section.

3. Governing equations for a cloud-topped mixed layer

In a nonsaturated mixed layer the dry static energy s and the water vapor mixing ratio q are constant with height up to the top of the mixed layer z_B, and the lifting condensation level z_C lies above z_B. In a cloud-topped mixed layer the moist static energy $h = c_pT + gz + Lq$ and the total water mixing ratio $q + l$ are constant with height up to the top of the mixed layer z_B, and the lifting condensation level z_C lies below z_B. If h and $q + l$ are constant with height in the mixed layer, it follows that the same is true for $s - Ll$. The temperature and moisture fields in the mixed layer are known if any two of the three quantities h, $q + l$ and $s - Ll$ are known. Although we shall occasionally use $s - Ll$, most of our discussion will be in terms of h and $q + l$.

The dependent variables of the cloud-topped mixed-layer model we shall now present are listed in the first column of Table 7. In addition, the required constants and externally specified parameters are listed in the second and third columns. The dependent variables are functions of the horizontal coordinates and time. We shall use a natural coordinate system in which x denotes distance in the downstream direction. The individual time derivative is then given by $\partial/\partial t + V(\partial/\partial x)$, where V is the speed of the horizontal wind. We shall assume that there is no turning of the wind with height and no change of wind speed with height. The horizontal projections of all trajectories are then coincident with the surface trajectories. We need not distinguish between winds at cloud top, in the mixed layer or at the surface.

a. Governing equations for the convective model

With the above assumptions the mixed-layer budgets of moist static energy and total water are

$$\frac{\partial h_M}{\partial t} + V\frac{\partial h_M}{\partial x} = \frac{(\overline{w'h'})_S - (\overline{w'h'})_B + F_S - F_B}{z_B}, \quad (3.1)$$

$$\frac{\partial (q + l)_M}{\partial t} + V\frac{\partial (q + l)_M}{\partial x} = \frac{(\overline{w'q'})_S - \overline{w'(q' + l')}_B}{z_B}. \quad (3.2)$$

These equations state that local changes of h_M and $(q + l)_M$ are caused by horizontal advection by the known wind V and by the vertical convergence of the convective and radiative fluxes. The turbulent fluxes are linear with height in the layer and jump to zero above z_B.

TABLE 7. Dependent variables, constants and externally specified parameters of the cloud-topped mixed-layer model.

Dependent variables		Constants		Externally specified parameters	
cloud-top height	z_B	see (3.11)	b	large-scale divergence	D
cloud-base height	z_C	specific heat at constant pressure	c_p	wind speed	V
mixed-layer moist static energy	h_M	bulk transfer coefficient	C_T	saturation moist static energy at sea surface temperature and pressure	h_S^*
mixed-layer total water mixing ratio	$(q+l)_M$	gravity	g	saturation mixing ratio at sea surface temperature and pressure	q_S^*
surface-moist static energy flux	$(\overline{w'h'})_S$	scale height	H	moist static energy just above cloud top	h_+
cloud-top moist static energy flux	$(\overline{w'h'})_B$	entrainment parameter	k	water vapor mixing ratio just above cloud top	q_+
surface water vapor flux	$(\overline{w'q'})_S$	latent heat of condensation	L	downward longwave flux just above cloud top	$LW_+^\downarrow$
cloud-top total water flux	$\overline{w'(q+l')_B}$	see (3.16)	β	total shortwave absorption	SW
cloud-top moist static energy jump	Δh	see (3.16)	γ		
cloud-top total water jump	$\Delta(q+l)$	see (3.13)	δ		
cloud-top temperature	T_B	see (3.16)	ϵ		
cloud-top jump in radiative flux	$F_+ - F_B$	density	ρ		
mixed-layer change in radiative flux	$F_B - F_S$	Stefan-Boltzmann constant	σ		
		longwave radiation partition	μ		
		shortwave radiation partition	μ'		

The surface turbulent fluxes of h and q are given by

$$(\overline{w'h'})_S = C_T V[h_S^* - h_M], \tag{3.3}$$

$$(\overline{w'q'})_S = C_T V[q_S^* - (q+l)_M]. \tag{3.4}$$

These equations relate the surface fluxes to the transfer coefficient C_T, the surface wind speed V, and the sea-air differences where h_S^* and q_S^* are the saturation values of h and q at the sea surface temperature and pressure.

Application of the budget equations for h and $q+l$ to the infinitesimally thin layer at the cloud top yields

$$\left(\frac{\partial z_B}{\partial t} + V\frac{\partial z_B}{\partial x} - w_B\right)\Delta h + (\overline{w'h'})_B = F_+ - F_B, \tag{3.5}$$

$$\left(\frac{\partial z_B}{\partial t} + V\frac{\partial z_B}{\partial x} - w_B\right)\Delta(q+l) + \overline{w'(q'+l')}_B = 0, \tag{3.6}$$

where w_B is the large-scale vertical velocity at z_B, Δh and $\Delta(q+l)$ are jumps across z_B, and $F_+ - F_B$ is the jump in the radiative flux across z_B. These equations are the cloud-top jump conditions on moist static energy and total water. When multiplied by the density ρ both (3.5) and (3.6) contain the quantity

$$\rho\left(\frac{\partial z_B}{\partial t} + V\frac{\partial z_B}{\partial x} - w_B\right),$$

which is the net mass flowing into the mixed layer per unit horizontal area per unit time. Such a mass flux into the mixed layer can be due to a local increase in the depth of the mixed layer with time, a horizontal flow across the top of the mixed layer when it deepens in the downstream direction, a large-scale subsidence, or more generally, a combination of these three effects. Nonturbulent air flowing into the mixed layer from above instantaneously changes its moist static energy by an amount Δh and its total water content by an amount $\Delta(q+l)$, where

$$\Delta h = h_+ - h_M, \tag{3.7}$$

$$\Delta(q+l) = q_+ - (q+l)_M, \tag{3.8}$$

h_+ and q_+ being known functions of z_B. According to (3.5), the instantaneous change in moist static energy is due to discontinuities in both the turbulent moist static energy flux and the radiative flux, while according to (3.6), the instantaneous change in total water content is due to a discontinuity in the turbulent total water flux.

Eqs. (3.5) and (3.6) can be regarded as predictive equations for z_B. In order that they predict z_B in a consistent manner,

$$\frac{L\Delta(q+l)}{\Delta h}(\overline{w'h'})_B - L\overline{w'(q'+l')}_B = \frac{L\Delta(q+l)}{\Delta h}(F_+ - F_B). \tag{3.9}$$

The cloud-base height z_C is approximately given in terms of the mixed-layer total water content $(q+l)_M$ and the saturation mixing ratio of the air just above the surface q_0^* as

$$\frac{z_C}{H} = \frac{q_0^* - (q + l)_M}{b} = \frac{(1 + \gamma)[q_S^* - (q + l)_M] - \frac{\gamma}{L}[h_S^* - h_M]}{b}, \tag{3.10}$$

where b is given by

$$b = \kappa\epsilon\gamma + p\left(\frac{\partial q^*}{\partial p}\right)_T, \tag{3.11}$$

ϵ and γ are defined in (3.16), and the scale height H and reference pressure p are assumed constant.

As was discussed in Section 2, Lilly (1968) argued that the turbulent energy balance sets maximum and minimum bounds on the entrainment. The entrainment assumption we shall use in the cloud-topped mixed-layer case is

$$\frac{k}{z_B}\int_0^{z_B} \overline{w's_v'}dz + \tfrac{1}{2}(1 - k)(\overline{w's_v'})_{\min} = 0, \tag{3.12}$$

where $\overline{w's_v'}$ is the turbulent flux of virtual dry static energy and $(\overline{w's_v'})_{\min}$ is the minimum value of this flux. Eq. (3.12) is identical to (2.3) except for the inclusion of virtual temperature effects.

If the effects of both water vapor and liquid water on buoyancy are included in the definition of the virtual dry static energy, then the virtual dry static energy s_v is related to the dry static energy s, the water vapor mixing ratio q and the liquid water mixing ratio l by

$$s_v = s + c_pT(\delta q - l), \tag{3.13}$$

where $\delta = 0.608$ and T is a constant reference temperature. Since $\overline{w'l'}$ vanishes in the subcloud layer while in the cloud layer $\overline{w'q'}$ and $\overline{w'h'}$ are related by

$$L\overline{w'q'} = \frac{\gamma}{1 + \gamma}\overline{w'h'} \quad \text{for} \quad z_C < z < z_B, \tag{3.14}$$

the turbulent virtual dry static energy flux can be expressed as

$$\overline{w's_v'} = \begin{cases} \beta\overline{w'h'} - \epsilon L\overline{w'(q' + l')}, & z_C < z < z_B \\ \overline{w'h'} - (1 - \epsilon\delta)L\overline{w'(q' + l')}, & 0 < z < z_C, \end{cases} \tag{3.15}$$

where

$$\beta = \frac{1 + \gamma\epsilon(\delta + 1)}{1 + \gamma}, \qquad \gamma = \frac{L}{c_p}\left(\frac{\partial q^*}{\partial T}\right)_p, \qquad \epsilon = \frac{c_pT}{L}. \tag{3.16}$$

Since h and $(q + l)$ are constant with height in the mixed layer, their turbulent fluxes must be linear functions of height so that

$$\overline{w'h'} = \left(1 - \frac{z}{z_B}\right)(\overline{w'h'})_S + \frac{z}{z_B}(\overline{w'h'})_B, \tag{3.17}$$

$$\overline{w'(q' + l')} = \left(1 - \frac{z}{z_B}\right)(\overline{w'q'})_S + \frac{z}{z_B}\overline{w'(q' + l')}_B. \tag{3.18}$$

Substitution of (3.15), (3.17) and (3.18) into (3.12) results in an expression which relates z_B, z_C, $(\overline{w'h'})_S$, $(\overline{w'h'})_B$, $(\overline{w'q'})_S$, and $\overline{w'(q' + l')}_B$:

$$\left\{\beta\left[1 - \left(\frac{z_C}{z_B}\right)^2\right] + \left(\frac{z_C}{z_B}\right)^2\right\}(\overline{w'h'})_B - \left\{\epsilon\left[1 - \left(\frac{z_C}{z_B}\right)^2\right] + (1 - \epsilon\delta)\left(\frac{z_C}{z_B}\right)^2\right\}L\overline{w'(q' + l')}_B + \left\{\beta\left(\frac{z_B - z_C}{z_B}\right)^2 + \left[1 - \left(\frac{z_B - z_C}{z_B}\right)^2\right]\right\}(\overline{w'h'})_S - \left\{\epsilon\left(\frac{z_B - z_C}{z_B}\right)^2 + (1 - \epsilon\delta)\left[1 - \left(\frac{z_B - z_C}{z_B}\right)^2\right]\right\}L(\overline{w'q'})_S + \left(\frac{1 - k}{k}\right)\min\left\{\begin{array}{c} \beta(\overline{w'h'})_B - \epsilon L\overline{w'(q' + l')}_B \\ \left[\frac{z_B - z_C}{z_B}(\overline{w'h'})_S + \frac{z_C}{z_B}(\overline{w'h'})_B\right] - (1 - \epsilon\delta)L\left[\frac{z_B - z_C}{z_B}(\overline{w'q'})_S + \frac{z_C}{z_B}\overline{w'(q' + l')}_B\right] \\ (\overline{w'h'})_S - (1 - \epsilon\delta)L(w'q')_S \end{array}\right\} = 0. \tag{3.19}$$

Since $\overline{w's_v'}$ is linear with height in the subcloud and cloud layers but discontinuous at cloud base, it would appear that the minimum in $\overline{w's_v'}$ could occur at the top of the cloud layer z_B, the bottom of the cloud layer z_{C+}, the top of the subcloud layer z_{C-}, or the bottom of the subcloud layer $z = 0$. However, the possibility of the minimum occurring at z_{C+} can be excluded by using (3.14), (3.15) and (3.16) to show that

$$(\overline{w's_v'})_{z_{C+}} - (\overline{w's_v'})_{z_{C-}}$$
$$= [1 - \epsilon(\delta - 1)]\left[L\overline{w'(q' + l')}_{z_C} - \frac{\gamma}{1+\gamma}(\overline{w'h'})_{z_C}\right]$$
$$= [1 - \epsilon(\delta + 1)]L(\overline{w'l'})_{z_{C+}}. \quad (3.20)$$

Since $[1 - \epsilon(\delta + 1)] > 0$ and $(\overline{w'l'})_{z_{C+}} > 0$, the virtual dry static energy flux is larger at z_{C+} than at z_{C-}, and only the remaining three possibilities are shown in the large braces of (3.19).

b. Governing equations for the radiative model

Boundary-layer convection is often driven by the upward virtual temperature flux from a warm underlying surface. However, in the stratocumulus regimes which border the cool coastal Bn climates, the virtual temperature flux at the surface is usually only weakly positive or is even negative, and yet the boundary layer is quite turbulent. Thus, cloud-topped mixed layers are often driven or at least partially driven not by heating from below but by cooling from above.

In considering cloud-topped mixed layers there arises the question of how much detail in the vertical profile of the radiative cooling can be included in Lilly's model. Our belief is that the model should be regarded as having two degrees of freedom in the vertical, e.g., as far as the h profile is concerned only h_M and z_B can change. Thus, the vertical profile of radiative cooling can have at most two degrees of freedom, i.e., radiative effects can appear in (3.1) and/or (3.5). Lilly's 1968 formulation is a simplified case since radiative cooling appears only in the cloud-top jump condition (3.5). Here we consider the more general situation where radiation appears in both (3.1) and (3.5). In Section 4 we shall investigate the sensitivity of the solutions to the partitioning of the radiative cooling between (3.1) and (3.5).

The radiative effects appearing in (3.1) and (3.5) are due to both longwave and shortwave radiation. Let us consider the longwave effects first. The net upward longwave flux LW can be expressed in terms of the upward flux $LW^{\uparrow}$ and the downward flux $LW^{\downarrow}$, i.e.,

$$LW = LW^{\uparrow} - LW^{\downarrow}. \quad (3.21)$$

To relate $LW^{\uparrow}$ and $LW^{\downarrow}$ to other model variables we first consider the Lilly (1968) formulation, which can be interpreted in terms of the idealized curves of $LW^{\uparrow}$ and $LW^{\downarrow}$ shown in Fig. 7. The downward longwave flux $LW^{\downarrow}$ changes sharply at cloud top, while the upward flux $LW^{\uparrow}$ changes considerably less sharply at cloud base. The net upward longwave flux LW is also shown in Fig. 7. The radiative cooling rate due to longwave radiation is given by $-(1/\rho c_p)(\partial LW/\partial z)$, the vertical profile of which is shown on the right of Fig. 7. If we neglect the warming near cloud base and the small cooling in the subcloud layer and if we assume $LW_+^{\uparrow}$ to be the blackbody flux at the cloud-top temperature, then, since $LW_B = LW_B^{\uparrow} - LW_B^{\downarrow} = 0$, we obtain

$$LW_+ - LW_B = \sigma T_B^4 - LW_+^{\downarrow}, \quad (3.22)$$
$$LW_B - LW_S = 0, \quad (3.23)$$

which we can regard as the Lilly (1968) formulation. In reality some of the longwave cooling probably extends into the mixed layer. We can incorporate this effect by simply assuming that the total longwave divergence across the mixed layer and the transition layer remains $\sigma T_B^4 - LW_+^{\downarrow}$, but that the fraction μ is partitioned to the mixed layer, i.e.

$$LW_+ - LW_B = (1 - \mu)(\sigma T_B^4 - LW_+^{\downarrow}), \quad (3.24)$$
$$LW_B - LW_S = \mu(\sigma T_B^4 - LW_+^{\downarrow}), \quad (3.25)$$

which reduce to (3.22) and (3.23) when $\mu = 0$.

The cloud top temperature T_B can be related to the model variables h_M, $(q + l)_M$, z_B and z_C as follows. The dry static energy at cloud top is equal to the dry static energy at cloud base plus the change which occurs when following a moist adiabat from cloud base to cloud top, i.e.,

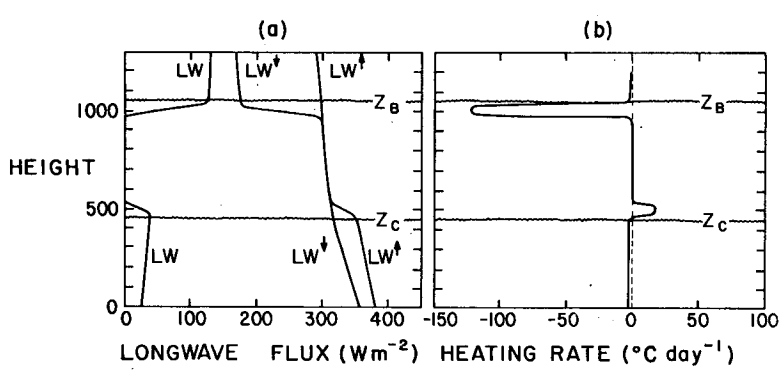

FIG. 7. (a) Idealized profiles of the upward and downward longwave radiative fluxes in and near a stratocumulus cloud. (b) Resulting heating rate. Values on the abscissa and ordinate are meant to be only roughly indicative.

$$s_B = s_C + \left(\frac{\partial s}{\partial z}\right)_{h^*}(z_B - z_C). \tag{3.26}$$

Since it can be shown that

$$\left(\frac{\partial s}{\partial z}\right)_{h^*} = \frac{L}{1+\gamma}\frac{b}{H}, \tag{3.27}$$

and since s_C is equal to $h_M - L(q + l)_M$, we can rewrite (3.26) as

$$T_B = \frac{1}{c_p}\left[h_M - L(q + l)_M + \frac{L}{1+\gamma}\frac{b}{H}(z_B - z_C) - gz_B\right]. \tag{3.28}$$

Eq. (3.28) gives the cloud-top temperature in terms of h_M, $(q + l)_M$, z_B and z_C.

A realistic treatment of the shortwave absorption requires consideration of the diurnal cycle. In the present study we wish to filter out the diurnal cycle and concentrate on the effects of varying sea surface temperature and large-scale divergence. Hence, for the total shortwave absorption SW we simply use the daily average value suggested by Lilly (1968), and partition the fraction μ' to the mixed layer.

We can now summarize the above discussion by writing

$$F_+ - F_B = \rho^{-1}\{(1-\mu)(\sigma T_B^4 - \mathrm{LW}_+^{\downarrow}) - (1-\mu')\mathrm{SW}\}, \tag{3.29}$$

$$F_B - F_S = \rho^{-1}\{\mu(\sigma T_B^4 - \mathrm{LW}_+^{\downarrow}) - \mu'\mathrm{SW}\}. \tag{3.30}$$

Thus, if μ, μ' and SW are specified constants, and if $\mathrm{LW}_+^{\downarrow}$ is a specified function of z_B, then $F_+ - F_B$ and $F_B - F_S$ can be computed from convective model variables by using (3.28), (3.29) and (3.30).

c. *Summary of the combined convective-radiative model*

The combined convective-radiative model consists of the surface flux relations (3.3) and (3.4), the cloud base relation (3.10), the definitions (3.7) and (3.8), the cloud-top temperature and radiation relations (3.28), (3.29) and (3.30), the entrainment assumption (3.19), the consistency relation (3.9), the mixed-layer budgets (3.1) and (3.2) and the cloud-top jump condition (3.5). These form a closed set of 13 equations in the 13 unknowns listed in the first column of Table 7. The constants and externally specified parameters required to integrate the model are listed in the second and third columns of Table 7. The governing equations of the combined convective-radiative model can now be arranged for numerical integration as follows:

$$(\overline{w'h'})_S = C_T V[h_S^* - h_M], \tag{3.31}$$

$$(\overline{w'q'})_S = C_T V[q_S^* - (q + l)_M], \tag{3.32}$$

$$\frac{z_C}{H} = \frac{(1+\gamma)[q_S^* - (q+l)_M] - \frac{\gamma}{L}[h_S^* - h_M]}{b}, \tag{3.33}$$

$$\Delta h = h_+ - h_M, \tag{3.34}$$

$$\Delta(q + l) = q_+ - (q + l)_M, \tag{3.35}$$

$$T_B = \frac{1}{c_p}\left[h_M - L(q+l)_M + \frac{Lb}{(1+\gamma)H}(z_B - z_C) - gz_B\right], \tag{3.36}$$

$$F_+ - F_B = \rho^{-1}\{(1-\mu)(\sigma T_B^4 - \mathrm{LW}_+^{\downarrow}) - (1-\mu')\mathrm{SW}\}, \tag{3.37}$$

$$F_B - F_S = \rho^{-1}\{\mu(\sigma T_B^4 - \mathrm{LW}_+^{\downarrow}) - \mu'\mathrm{SW}\}, \tag{3.38}$$

$$\begin{bmatrix} a_{11} & a_{12} \\ a_{21} & a_{22} \end{bmatrix}\begin{bmatrix} (\overline{w'h'})_B \\ L\overline{w'(q'+l')}_B \end{bmatrix} = \begin{bmatrix} b_1 \\ b_2 \end{bmatrix}, \tag{3.39}$$

(3.40)

$$\frac{dh_M}{dt} = \frac{(\overline{w'h'})_S - (\overline{w'h'})_B + F_S - F_B}{z_B}, \tag{3.41}$$

$$\frac{d(q+l)_M}{dt} = \frac{(\overline{w'q'})_S - \overline{w'(q'+l')}_B}{z_B}, \tag{3.42}$$

$$\frac{dz_B}{dt} = -Dz_B + \frac{F_+ - F_B - (\overline{w'h'})_B}{\Delta h}. \tag{3.43}$$

Eqs. (3.39) and (3.40) are simply a shorthand notation for (3.19) and (3.9). Given initial conditions on h_M, $(q + l)_M$ and z_B, the system (3.31)–(3.43) can be numerically integrated. A single computation cycle is as follows:

1) Compute the surface fluxes $(\overline{w'h'})_S$ and $(\overline{w'q'})_S$ from (3.31) and (3.32).

2) Compute cloud base z_C from (3.33).

3) Compute the cloud-top jumps in moist static energy and total water from (3.34) and (3.35).

4) Compute the cloud-top temperature from (3.36) and then the radiative flux differences from (3.37) and (3.38).

5) Compute the cloud top fluxes $(\overline{w'h'})_B$ and $\overline{w'(q'+l')}_B$ from the two-by-two system (3.39) and (3.40).

6) Predict new values of h_M, $(q + l)_M$ and z_B from (3.41), (3.42) and (3.43).

The above procedure is straightforward except for step 5. The two by two system (3.39)–(3.40) relates z_B, z_C, $(\overline{w'h'})_S$, $(\overline{w'h'})_B$, $(\overline{w'q'})_S$, $\overline{w'(q'+l')}_B$, Δh, $\Delta(q + l)$ and $F_+ - F_B$. When beginning step 5 we regard z_B, z_C, $(\overline{w'h'})_S$, $(\overline{w'q'})_S$, Δh, $\Delta(q + l)$ and $F_+ - F_B$ as known. Then (3.39)–(3.40) can be regarded as two equations in the two unknowns $(\overline{w'h'})_B$ and $\overline{w'(q'+l')}_B$. However, because of the

form of (3.19), the coefficient matrix and the right-hand side column vector in (3.39)–(3.40) are unknown until the location of the minimum $\overline{w's_v'}$ is known, i.e., until $(\overline{w'h'})_B$ and $\overline{w'(q'+l')}_B$ are known. Thus (3.39)–(3.40) have a somewhat implicit form. Our procedure is to first assume that the minimum $\overline{w's_v'}$ occurs at z_B, solve (3.39)–(3.40) for $(\overline{w'h'})_B$ and $\overline{w'(q'+l')}_B$, then, using (3.15), check to see if the minimum $\overline{w's_v'}$ actually occurs at z_B. This procedure is repeated for assumptions that the minimum $\overline{w's_v'}$ occurs at z_{C-} and at the surface. If one and only one of these three possibilities does not lead to a contradiction, we have found the unique solution. It is possible that no solution exists or that more than one solution exists. We have not encountered any problems with existence or uniqueness and have found minimum $\overline{w's_v'}$ fluxes at either the top of the subcloud layer or at the surface.

In Part II of this study we shall use the above procedure to numerically integrate the system (3.31)–(3.43) under varying sea surface temperature and large-scale divergence. But before studying the horizontally inhomogeneous solutions let us gain deeper insight into model behavior by considering horizontally homogeneous steady-state solutions.

4. Horizontally homogeneous steady-state solutions

Under steady-state horizontally homogeneous conditions the turbulent flux of $q+l$ is constant with height. Thus, we can omit the subscript notation from $\overline{w'(q'+l')}$. The subscript notation must be retained on $\overline{w'h'}$ because of mixed-layer radiation and on $\overline{w's_v'}$ both because of mixed-layer radiation and the discontinuity of $\overline{w's_v'}$ at cloud base. In this section it will prove useful to linearize the σT_B^4 on the right-hand side of (3.37) and (3.38), so that

$$\sigma T_B^4 \approx \sigma T_0^4 \left[1 + \frac{4}{T_0}(T_B - T_0)\right], \quad (4.1)$$

where T_0 is a constant reference temperature. Typically, the linearization of the blackbody flux results in an underestimate of the upward flux σT_B^4 of less than 1% for cloud-top temperatures within 10°C of the reference temperature.

Eqs. (3.1), (3.3), (3.4), (3.5), (3.7), (3.10) and (3.28) can now be combined to give

$$(\overline{w'h'})_S = \left[1 + \frac{C_T V}{Dz_B} + \frac{4\sigma T_0^3}{(1+\gamma)\rho c_p D z_B}\right]^{-1} C_T V \times \left\{h_S^* - h_+ + \frac{1}{\rho D z_B}\left\{\sigma T_0^4 + 4\sigma T_0^3 \times \left[T_S - T_0 + \left(\frac{Lb}{(1+\gamma)gH} - 1\right)\frac{g}{c_p} z_B\right] - \mathrm{LW}_+^{\downarrow} - \mathrm{SW}\right\}\right\}, \quad (4.2)$$

where T_S is the sea surface temperature. Eq. (3.1) becomes

$$(\overline{w'h'})_B = \left[1 + \frac{\mu 4\sigma T_0^3}{(1+\gamma)\rho c_p C_T V}\right](\overline{w'h'})_S - \frac{\mu}{\rho}\left\{\sigma T_0^4 + 4\sigma T_0^3\left[T_S - T_0 + \left(\frac{Lb}{(1+\gamma)gH} - 1\right)\frac{g}{c_p} z_B\right] - \mathrm{LW}_+^{\downarrow}\right\} + \frac{\mu'}{\rho}\,\mathrm{SW}, \quad (4.3)$$

while (3.4), (3.6) and (3.8) combine to give

$$L\overline{w'(q'+l')} = \left(1 + \frac{C_T V}{Dz_B}\right)^{-1} C_T V L(q_S^* - q_+). \quad (4.4)$$

With the help of (3.3) and (3.4), the cloud-base relation (3.10) can be written

$$\frac{z_C}{H} = (LbC_T V)^{-1}[(1+\gamma)L\overline{w'(q'+l')} - \gamma(\overline{w'h'})_S]. \quad (4.5)$$

From (3.17) the moist static energy flux at cloud base is given by

$$(\overline{w'h'})_C = \left(1 - \frac{z_C}{z_B}\right)(\overline{w'h'})_S + \frac{z_C}{z_B}(\overline{w'h'})_B, \quad (4.6)$$

while the turbulent fluxes of virtual dry static energy just below cloud top, just above cloud base, just below cloud base and at the surface are respectively given by

$$(\overline{w's_v'})_B = \beta(\overline{w'h'})_B - \epsilon L\overline{w'(q'+l')}, \quad (4.7)$$

$$(\overline{w's_v'})_{C+} = \beta(\overline{w'h'})_C - \epsilon L\overline{w'(q'+l')}, \quad (4.8)$$

$$(\overline{w's_v'})_{C-} = (\overline{w'h'})_C - (1-\epsilon\delta)L\overline{w'(q'+l')}, \quad (4.9)$$

$$(\overline{w's_v'})_S = (\overline{w'h'})_S - (1-\epsilon\delta)L\overline{w'(q'+l')}. \quad (4.10)$$

As long as the minimum s_v flux occurs at z_{C-}, the entrainment relation (3.12) takes the form

$$\frac{1-k}{k}(\overline{w's_v'})_{C-} + (\overline{w's_v'})_B + (\overline{w's_v'})_{C+} + \frac{z_C}{z_B}(\overline{w's_v'})_S + (\overline{w's_v'})_{C-} - (\overline{w's_v'})_B - (\overline{w's_v'})_{C+}] = 0. \quad (4.11)$$

Eqs. (4.2)–(4.11) can be regarded as a closed system in the unknowns z_B, z_C, $(\overline{w'h'})_B$, $(\overline{w'h'})_C$, $(\overline{w'h'})_S$, $\overline{w'(q'+l')}$, $(\overline{w's_v'})_B$, $(\overline{w's_v'})_{C+}$, $(\overline{w's_v'})_{C-}$ and $(w's_v')_S$. In order to reduce this system to a single equation in z_B, we could use (4.7)–(4.10) to eliminate the virtual dry static energy fluxes from (4.11), then use (4.2)–(4.6) to eliminate $(\overline{w'h'})_S$, $(\overline{w'h'})_B$, $\overline{w'(q'+l')}$, z_C and $(\overline{w'h'})_C$. The resulting equation for z_B is implicit, and, due to its complicated form,

is not presented here. We have instead chosen to compute solutions to the system (4.2)–(4.11) in the following manner:

1) Make an initial estimate for z_B.

2) From the current estimate of z_B, compute in sequence $(\overline{w'h'})_S$, $(\overline{w'h'})_B$, $\overline{w'(q'+l')}$, z_C, $(\overline{w'h'})_C$, $(\overline{w's_v'})_B$, $(\overline{w's_v'})_{C+}$, $(\overline{w's_v'})_{C-}$ and $(\overline{w's_v'})_S$ from (4.2)–(4.10).

3) If (4.11) is satisfied to within some tolerable error, a solution has been obtained. If not, use the secant method on (4.11) to make an improved estimate of z_B and return to step 2.

We have used this method to compute horizontally homogeneous steady-state solutions for sea surface temperatures between 13 and 18°C and large-scale divergences between 1×10^{-6} and 6×10^{-6} s^{-1}. For those constants which require a reference temperature and/or pressure we have used a reference temperature 4.5°C colder than the sea surface temperature and a reference pressure 4.5 kPa lower than the surface pressure, which is assumed to be 102 kPa. Typical values of the constants are listed in the left column of Table 8. Values of the externally specified parameters are listed in the right column of the table. The functions h_+ and q_+ were determined from the mean July 1967–70 Oakland sounding (U. S. Dept. of Commerce, 1967–70). The function $LW_+^\downarrow$ was determined by using the same mean July Oakland sounding as input to the longwave transfer model of Cox (1973). For SW we have used the daily average suggested by Lilly (1968).

The results for the horizontally homogeneous steady-state case with $k = 0.2$ and $\mu = \mu' = 0$ are shown by the solid curves in Figs. 8–12, while results for the case with $k = 0.2$ and $\mu = \mu' = 0.2$ are shown by the dashed curves for those fields where significant differences exist. These figures show isopleths of the various model outputs as functions of the large-scale divergence and sea surface temperature. Fig. 8a shows that the boundary layer deepens as the large-scale divergence decreases and the sea surface temperature increases. Roughly speaking (see Schubert, 1976, Section 3), the boundary-layer depth is inversely proportional to the large-scale divergence so that halving the divergence approximately doubles the depth of the boundary layer. Thus, when the large-scale divergence is changed the mixed-layer depth changes until an approximately equal cloud-top subsidence rate is found (i.e., Dz_B is approximately invariant). Fig. 8b shows the cloud-base height, which increases as the large-scale divergence decreases and the sea surface temperature increases. The variation of cloud-base height is much less than cloud-top height so that the appearance of the cloud thickness field is remarkably similar to that of the cloud-top field. As might be expected the effect of taking some of the radiative cooling out of the transition layer and using it to cool the mixed layer is to decrease both z_B and z_C.

The total radiative forcing across the mixed layer and transition layer, $\sigma T_B^4 - LW_+^\downarrow - SW$, is shown in Fig. 9. The upward longwave flux off cloud top depends on T_B, which in turn depends on h_M, $(q+l)_M$, z_C and z_B as given by (3.28). Most of the variation of σT_B^4 is simply related to the fact that T_B decreases as cloud top increases. $LW_+^\downarrow$ is simply a linear function of z_B as given in Table 8. Since $LW_+^\downarrow$ decreases with z_B faster than σT_B^4 does, the total radiative forcing $\sigma T_B^4 - LW_+^\downarrow - SW$ increases as z_B increases. The total radiative forcing for the $\mu = 0.2$ case (not shown) is slightly smaller than the $\mu = 0$ case. The difference is less than 1 W m^{-2} over most of the diagram.

Fig. 10 shows the dependence of the mixed-layer moist static energy and total water mixing ratio on the divergence and sea surface temperature. Except

TABLE 8. Constants and externally specified parameters. For those constants which depend on a reference temperature and/or pressure, only typical values are given.

Constants	Externally specified parameters
$c_p = 1004.5$ J kg^{-1} K^{-1}	$1 \times 10^{-6} \leq D \leq 6 \times 10^{-6}$ s^{-1}
$C_T = 0.0015$	$V = 7$ m s^{-1}
$g = 9.80$ m s^{-2}	$310.29 \leq h_S^* \leq 324.13$ J kg^{-1}
$k = 0.2$	$9.27 \leq q_S^* \leq 12.8$ g kg^{-1}
$\delta = 0.608$	$h_+ = 314.4 + 0.00187\, z_B$ (kJ kg^{-1})
$\sigma = 5.67 \times 10^{-8}$ W m^{-2} K^{-4}	$q_+ = 4.38 - 0.000614\, z_B$ (g kg^{-1})
	$LW_+^\downarrow = 339.4 - 0.0398\, z_B$ (W m^{-2})
Constants which depend on reference temperature and/or pressure	SW = 22.3 W m^{-2}
$b = 0.0359$	
$H = 8307$ m	
$L = 2.47 \times 10^6$ J kg^{-1}	
$\beta = 0.533$	
$\gamma = 1.34$	
$\epsilon = 0.115$	
$\rho = 1.22$ kg m^{-3}	

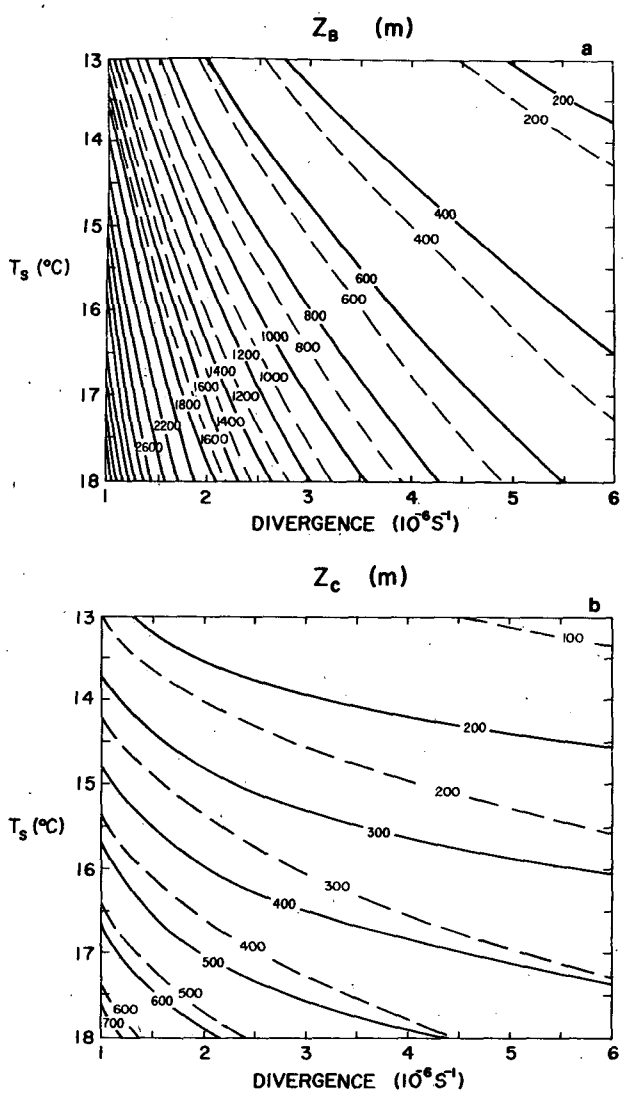

FIG. 8. Isopleths of (a) the cloud-top height z_B and (b) the cloud-base height z_C for various large-scale divergences and sea surface temperatures. The solid curves are for $\mu = \mu' = 0$ and the dashed curves for $\mu = \mu' = 0.2$. All other externally specified parameters and constants are given in Table 8.

for very small divergences both h_M and $(q + l)_M$ are fairly independent of the divergence. Since the $\mu = 0.2$ case has less entrainment of dry air (lower z_B) the surface evaporation need not be as high, i.e., $(q + l)_M$ need not be so low. For the $\mu = 0.2$ case $(q + l)_M$ averages about 0.1 g kg^{-1} higher than the $\mu = 0$ case. h_M for the two cases is essentially identical.

The cloud-top jumps of moist static energy and temperature are shown in Fig. 11. Once again, the results for $\mu = 0.2$ do not differ from the results for $\mu = 0$. The temperature inversion at cloud-top tends to be quite large (between 8 and 16°C). However, even with such strong temperature inversions the extremely dry air above cloud-top can lead to a negative jump in the moist static energy across cloud-top. As discussed by Lilly (1968), a cloud-topped mixed layer with $\Delta h < 0$ is possibly unstable. A crude argument, which neglects virtual temperature effects, is as follows. If a parcel of air just above z_B with moist static energy $h_+ < h_M$ is displaced downward across z_B and mixed with a parcel of cloud layer air with moist static energy h_M, the resulting parcel has intermediate moist static energy, $h_+ < h_{\text{parcel}} < h_M$. If the resulting parcel is saturated, the difference between h_{parcel} and h_M (which is equal to h^* in the cloud layer) is proportional to the temperature difference between parcel and environment, i.e., the parcel buoyancy. Since $h_{\text{parcel}} < h_M$, negative buoyancy and instability results. Thus, results with $\Delta h < 0$ must be interpreted with caution. A more accurate stability condition, which includes virtual temperature effects, has been given by Randall (1979a). His conclusion is that instability does not begin until Δh is appreciably negative, on the order of -2 kJ kg^{-1} in the present case. Fig. 11a indicates that, with the external parameters specified in Table 8, stable horizontally homogeneous steady-state stratocumulus clouds are probably limited to conditions with sea surface temperatures colder than about 17–18°C.

The turbulent fluxes of moist static energy, total water and virtual dry static energy are shown in Fig. 12. The surface flux of moist static energy (Fig. 12a) and the flux of total water (Fig. 12b) are fairly independent of divergence except for small values of divergence. For the $\mu = 0$ case total water flux everywhere exceeds the moist static energy flux, which leads to a negative flux of liquid water static energy, i.e., a negative heat flux at the surface. There is considerable increase in both $\rho\overline{w'h'}$ and

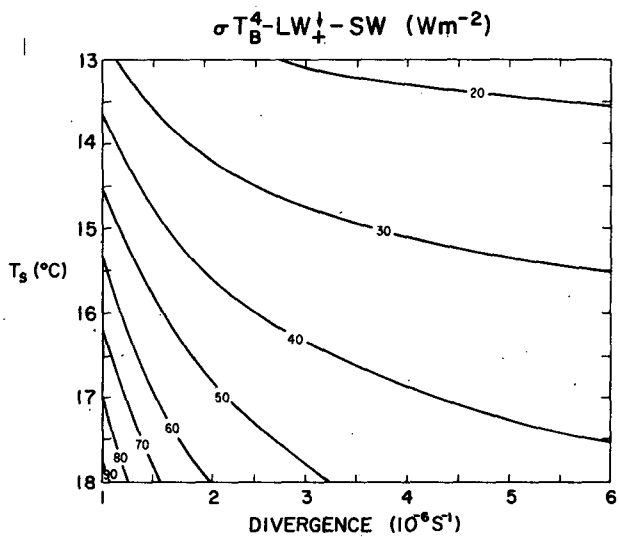

FIG. 9. Isopleths of the net radiative flux divergence across the mixed layer and the transition layer.

$\rho L\overline{w'(q' + l')}$ as sea surface temperature increases. The cloud top and surface fluxes of virtual dry static energy (Figs. 12c and 12d) are simply computed from (4.7) and (4.10). The subcloud layer flux is weak and often negative and there is a considerable jump to positive values of virtual dry static energy flux in the cloud layer.

The virtual dry static energy flux is not the only flux which is discontinuous across cloud base. The heat flux $\overline{w's'}$, the water vapor flux $\overline{w'q'}$ and the liquid water flux $\overline{w'l'}$ are all discontinuous across cloud base as can easily be seen through the use of (3.14). Although the three basic fluxes $\overline{w's'}$, $\overline{w'q'}$ and $\overline{w'l'}$ are all discontinuous across z_C, they are discontinuous in such a way that $\overline{w'h'}$, $L\overline{w'(q' + l')}$ and hence $\overline{w'(s' - Ll')}$ are continuous across z_C, as shown schematically in Fig. 13 for the $\mu = 0$ case.

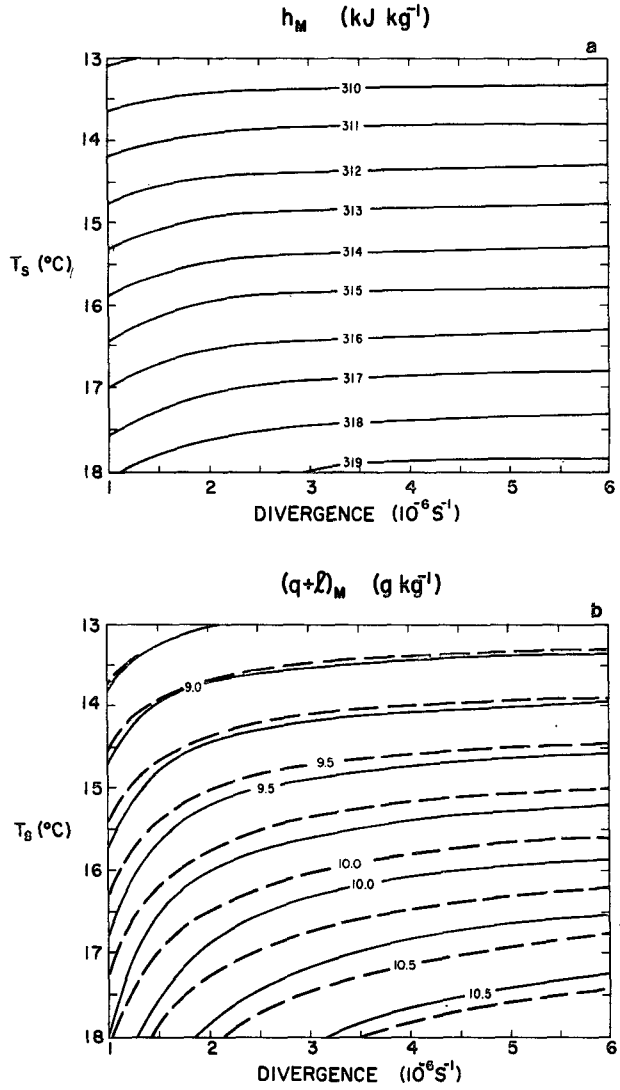

FIG. 10. Isopleths of (a) the mixed-layer moist static energy h_M and (b) the mixed-layer total water mixing ratio $(q + l)_M$.

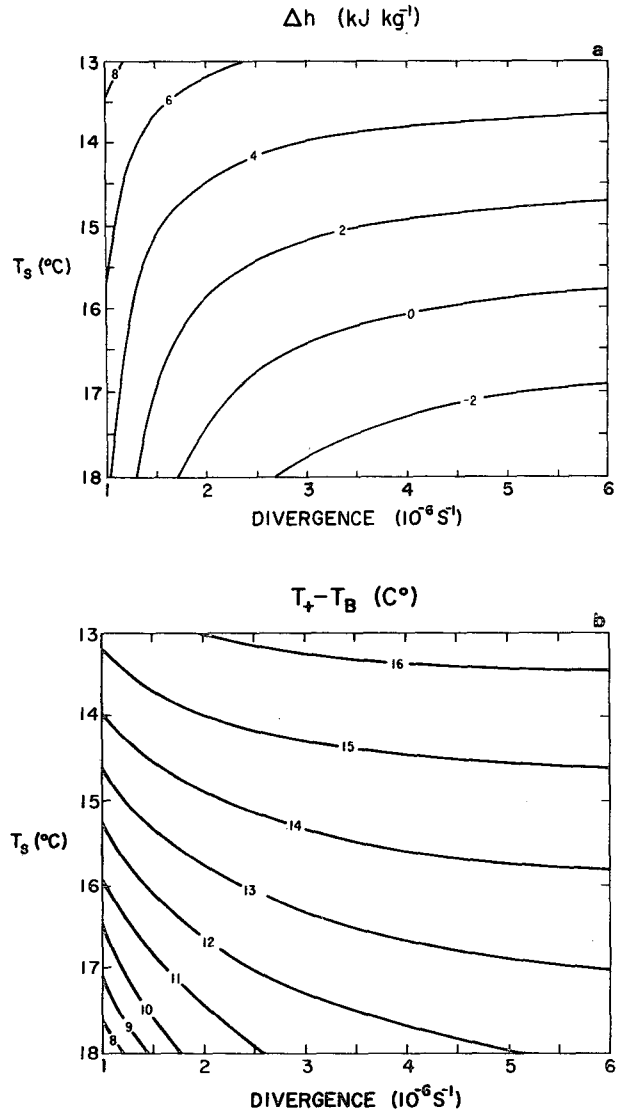

FIG. 11. Isopleths of the cloud top jumps of (a) moist static energy and (b) temperature. The possibility of instability (see text) exists in the region where $\Delta h < 0$.

The turbulent flux discontinuities across z_B are readily understandable since the turbulent fluxes in the air above z_B must vanish. However, understanding the turbulent flux discontinuities across z_C is more difficult since these discontinuities are not accompanied by discontinuities in s, q or l. For example, since $L\overline{w'q'}$ jumps to a lower value and $L\overline{w'l'}$ jumps from zero to a positive value across z_C, there is a finite amount of condensation in the infinitesimally thin layer centered at cloud base. The net condensation at cloud base is balanced by the net evaporation at cloud top. This may at first sight seem strange, but it can be understood in terms of a convective element model. Although a convective element model is not explicit in the theory, let us

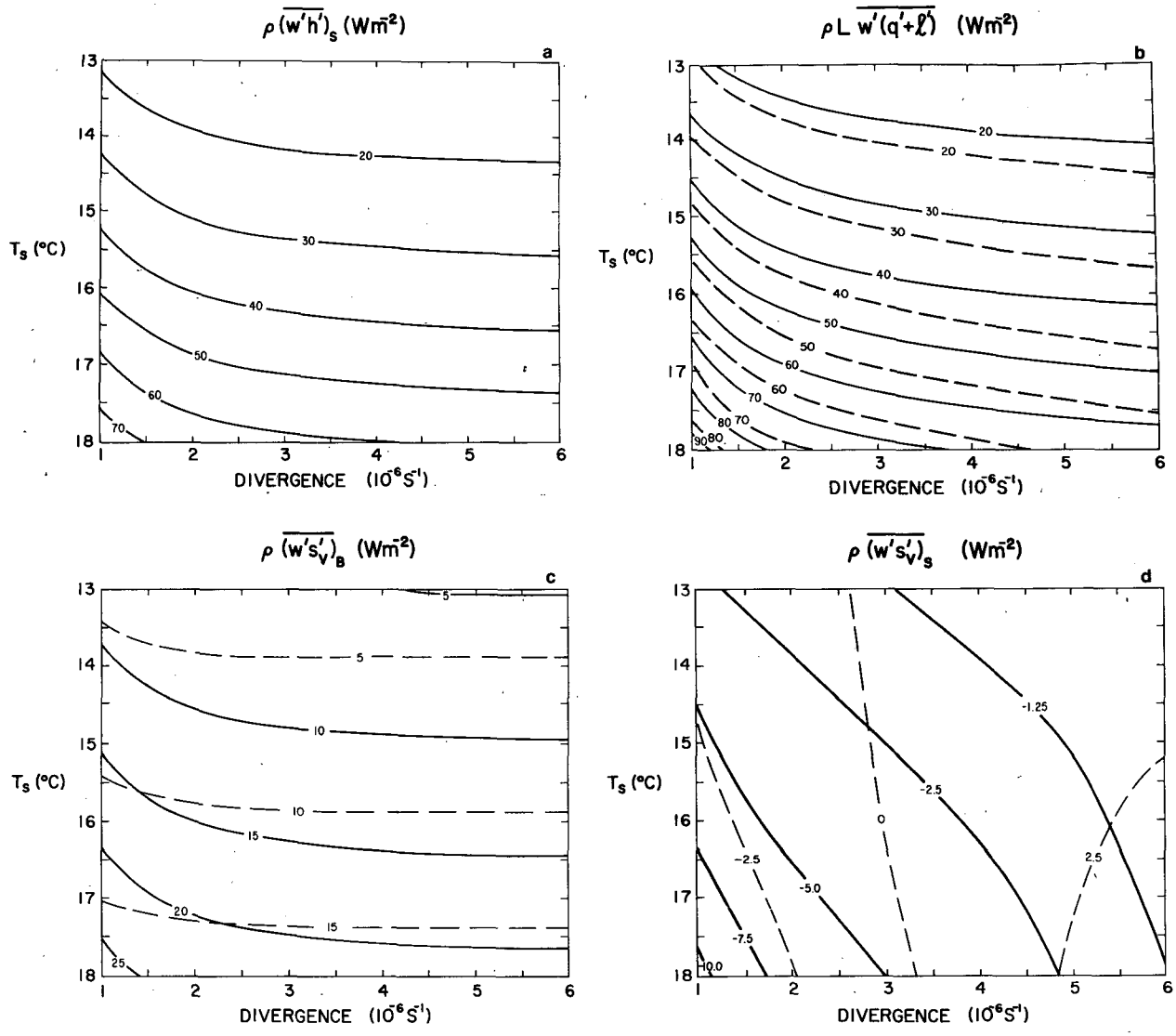

FIG. 12. Isopleths of the turbulent fluxes of (a) moist static energy $\rho(\overline{w'h'})_S$, (b) total water $\rho L\overline{w'(q' + l')}$, (c) virtual dry static energy at cloud top $\rho(\overline{w's_v'})_B$ and (d) virtual dry static energy at the surface $\rho(\overline{w's_v'})_S$.

proceed to interpret the jumps in $\overline{w's'}$, $L\overline{w'q'}$, and $L\overline{w'l'}$ at z_C in terms of such a model.

Consider a parcel of air which is circulating in the mixed layer and which is exposed to radiative cooling only near cloud top ($\mu = 0$). Figs. 14 and 15 illustrate schematically the parcel paths of the energy and moisture parameters and their associated fluxes. The conservative quantities h and $(q + l)$ (and their difference $s - Ll$) are shown in Fig. 14. The nonconservative quantities s, q and l, which are somewhat more complicated, are shown in Fig. 15. As the parcel ascends along a dry adiabat from the ocean surface it conserves s, q and l (which is zero) until it reaches z_{C-}, a point just below z_C. At this point, the parcel is saturated and its further ascent is along a wet adiabat. Along the wet adiabat s and l increase and q decreases, all in such a way that h, $(q + l)$ and $(s - Ll)$ are conserved. When the saturated and water bearing parcel crosses z_B, it mixes with some of the warm and dry air above z_B. The warmth of the entrained air tends to warm the parcel but its dryness tends to cool the parcel by evaporating enough liquid water to maintain saturation. In addition to this evaporative cooling, the parcel is also cooled radiatively since the air below is cloudy and the air above is clear. The sum of the evaporative and radiative cooling overwhelms the entrainment warming and the parcel begins descent along a wet adiabat at a lower temperature, a lower water vapor mixing ratio and a lower liquid water mixing ratio. Since the liquid water mixing ratio is lower, the wet adiabatic

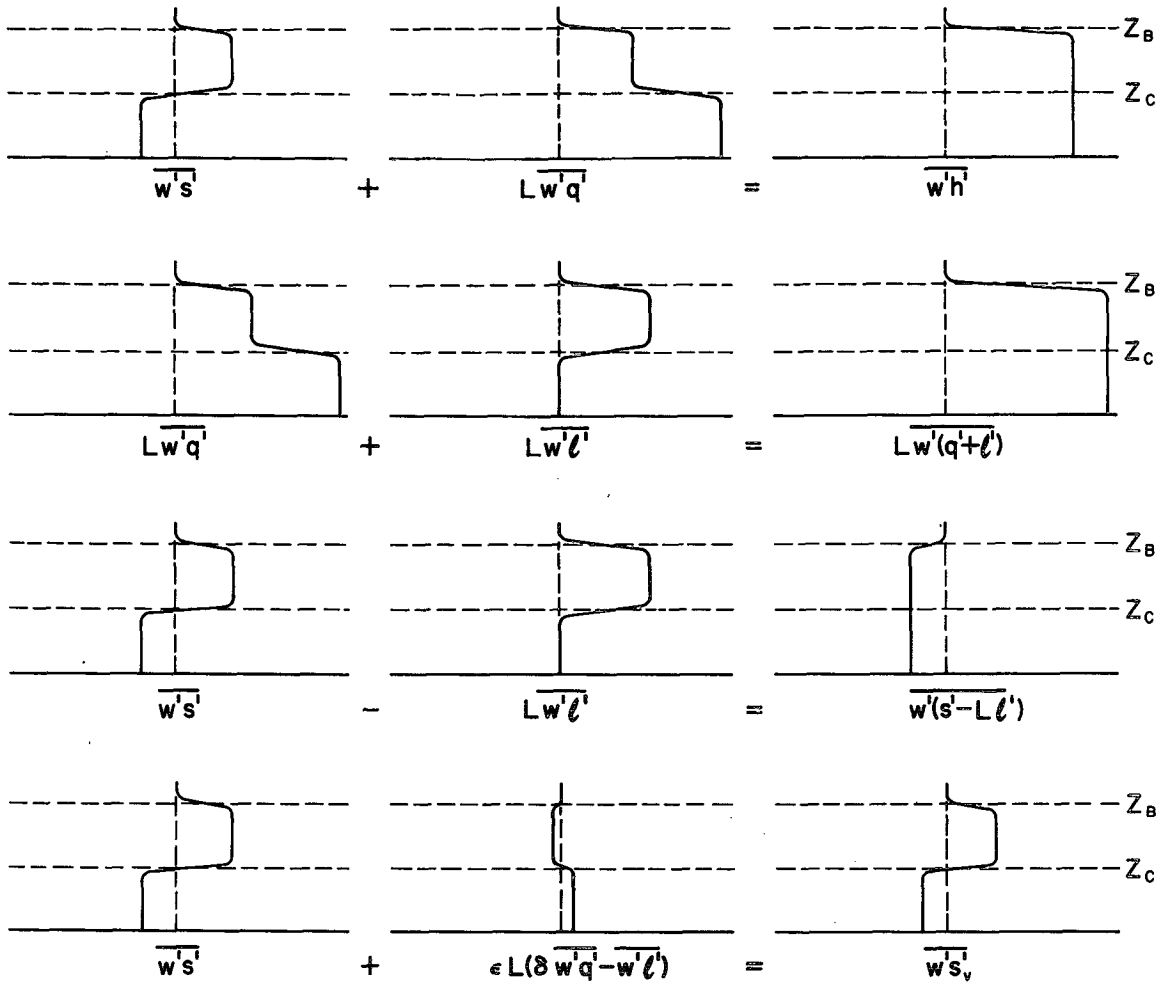

FIG. 13. Profiles of the three basic fluxes $\overline{w's'}$, $L\overline{w'q'}$ and $L\overline{w'l'}$ and their combinations to form $\overline{w'h'}$, $L\overline{w'(q' + l')}$ and $\overline{w'(s' - Ll')}$. These profiles are typical of steady-state horizontally homogeneous conditions when $\mu = \mu' = 0$.

descent cannot continue to z_{C-} but terminates at z_{C+}, a point just above z_C. Descent below z_{C+} is along a dry adiabat with s, q and l (which is again zero) being conserved. On arriving at the surface, the descending parcel gives up heat to the ocean and receives water vapor from the ocean and then begins another circuit.

If the mixed layer is horizontally homogeneous and is in a locally steady state, every parcel circuit is identical. This is the situation illustrated in Figs. 13–15. If the mixed layer is not horizontally homogeneous or is not in a locally steady state, parcel circuits are not identical and the mixed layer may be changing its h_M, $(q + l)_M$, z_B, etc. We shall discuss the horizontally inhomogeneous situation further in Part II of this study.

A prediction of the horizontally homogeneous steady-state theory with $\mu = 0$ is that $\overline{w's'_v}$ is negative below cloud base, i.e., upward moving parcels in the subcloud layer are virtually colder than downward moving parcels at the same level. If upward moving subcloud layer parcels are negatively buoyant, how are they accelerated upward from the sea surface? The answer to this question must lie in the pressure field associated with the convective cells. Under the anelastic approximation this nonhydrostatic pressure field can be computed from a diagnostic equation if the temperature and motion fields are known [e.g., Eq. (32) of Ogura and Phillips, 1962; or Eq. (2.4) of Arnason *et al.*, 1968]. This pressure field, along with the associated temperature, motion, cloud-base and cloud-top fields, are shown schematically in Fig. 16. Air near the surface is accelerated toward the updraft and upward against negative buoyancy by lower pressure in the updraft near cloud base. If one computes the correlation of this pressure pattern with the convective-scale vertical motion field, one finds $(\overline{w'p'})_{z=z_C}$

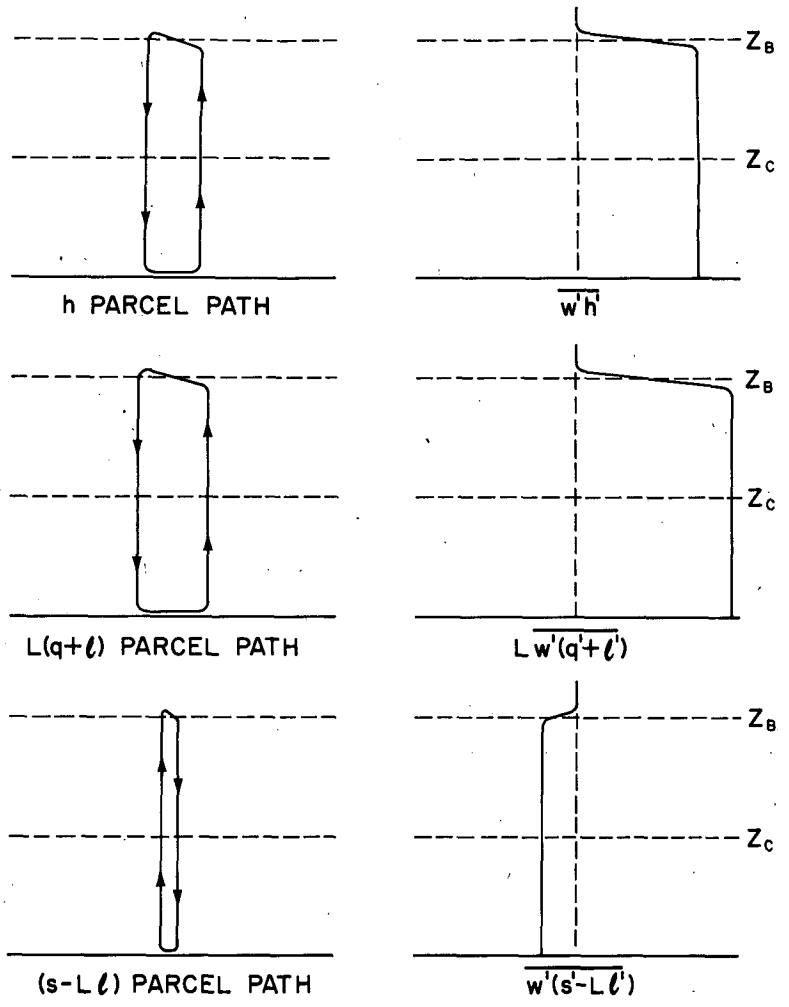

FIG. 14. Typical parcel paths of the conservative quantities h, $L(q + l)$ and $s - Ll$ and the resulting fluxes $\overline{w'h'}$, $L\overline{w'(q' + l')}$ and $\overline{w'(s' - Ll')}$.

< 0. In other words, the work done on the subcloud layer by the cloud layer maintains the convection motions of the subcloud layer.

The horizontally homogeneous steady-state solutions we have just discussed must be applied with caution to real physical situations. This fact will become clear in Part II where we will show that certain aspects (especially of cloud-top) of the solutions found under steady-state horizontally advective situations can be far from their steady-state horizontally homogeneous values.

5. Summary and conclusions

The most persistent low-level stratocumulus clouds appear to occur over the eastern Pacific and Atlantic Oceans during the Northern Hemisphere summer. These clouds overlie cool ocean currents and are associated with the trade winds to the east of the semipermanent subtropical high-pressure cells. Bordering these marine stratocumulus clouds are the "foggy deserts" or Bn climates. A more turbulent type of cloud-topped mixed layer occurs during the wintertime outbreak of cold air over a relatively warm ocean.

In this paper we have slightly generalized Lilly's (1968) model of such cloud-topped mixed layers. The generalization is in three directions: 1) horizontal advection has been included; 2) a simple radiative model, which includes mixed layer cooling, has been coupled to the convective model, the coupling existing because the downward longwave flux at cloud top depends on cloud-top height and because the upward longwave flux off cloud top depends on cloud-top temperature; and 3) a weighted average of Lilly's maximum and minimum entrainment assumptions has been used. Since our entrainment assumption takes a somewhat implicit form,

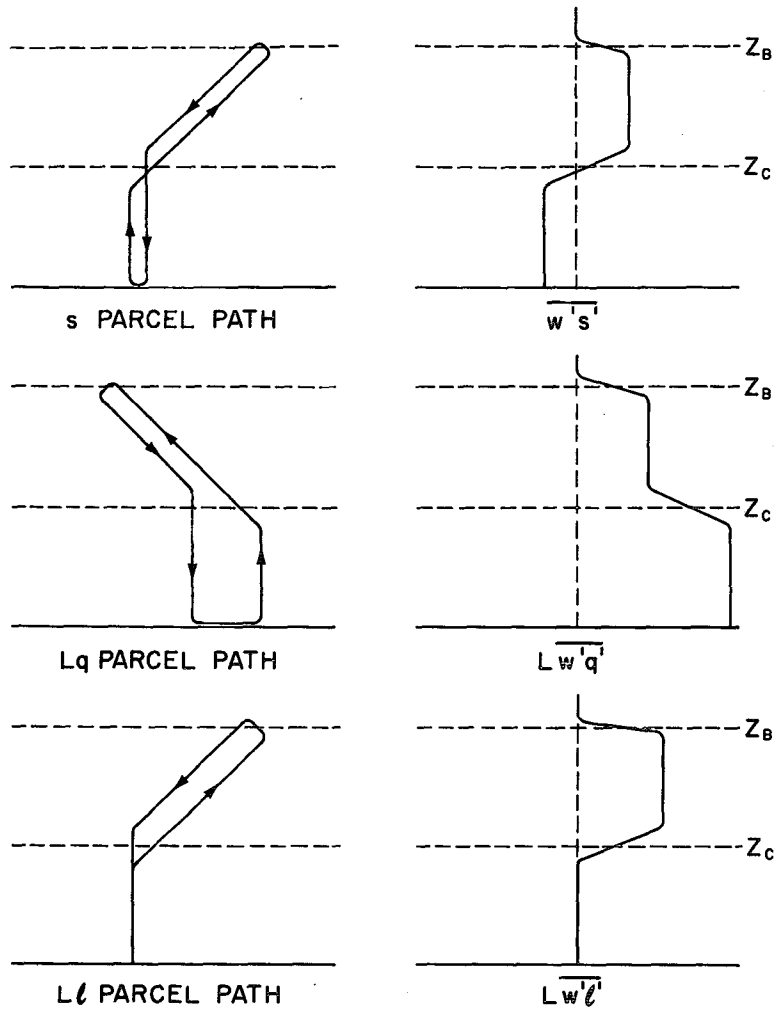

FIG. 15. Typical parcel paths of the nonconservative quantities s, Lq and Ll and resulting fluxes $\overline{w's'}$, $\overline{Lw'q'}$ and $\overline{Lw'l'}$. Note that in the major portion of the cloud there is no net condensation and $\overline{Lw'l'}$ is constant with height. The net condensation at cloud base is balanced by the net evaporation at cloud top.

to illustrate its use we have presented in Section 2 some integrations of the simple dry "cloud" model. The procedure for integrating the more complicated moist case has been presented in Section 3, but before presenting integrations of the horizontally inhomogeneous moist case (see Part II) we have studied in Section 4 the horizontally homogeneous steady-state solutions.

Under horizontally homogeneous steady-state conditions the governing equations reduce to a system of nonlinear algebraic equations which we have solved by an iterative method. We have computed solutions for sea surface temperatures between 13 and 18°C and large-scale divergences between 1×10^{-6} and 6×10^{-6} s^{-1}. An interesting feature of these solutions is that the large-scale divergence plays an important role in determining the cloud-top height but practically no role in determining the temperature and moisture profiles below cloud top. The partitioning of some of the radiative cooling to the mixed layer lowers both cloud top and cloud base and can have important quantitative effects. However, the general pattern of mixed-layer response to sea surface temperature and large-scale divergence is not highly sensitive to the radiation partition.

According to the model the fluxes of heat, water vapor and liquid water are discontinuous across cloud base. These discontinuities can be interpreted in terms of convective parcel paths if we relax our view of cloud base z_C to allow upward moving parcels to have cloud base z_{C-} and downward moving parcels to have cloud base z_{C+}, the difference being due to the evaporation by mixing of dry

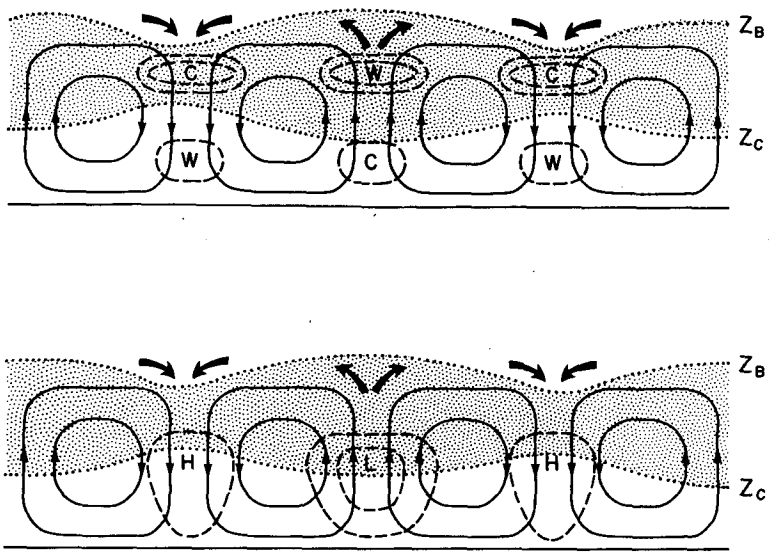

FIG. 16. Schematic depiction of the motion field of a convective element along with its associated cloud-base, cloud-top, temperature (top) and nonhydrostatic pressure (bottom) fields. Note that the updraft has positive buoyancy in the cloud layer and negative bouyancy below. To accelerate surface air upward into the updraft requires the nonhydrostatic pressure shown. Since $\overline{w'p'} < 0$ at cloud base, the cloud layer does work on the subcloud layer.

air from above cloud top. There is then net condensation at cloud base and net evaporation at cloud top. The positive heat flux in the cloud layer and negative heat flux in the subcloud layer imply that parcels are forced to circulate through the subcloud layer against adverse buoyancy. This emphasizes the important role of nonhydrostatic pressure forces in maintaining the convection, i.e., the cloud layer does work on the subcloud layer. One might imagine that convective cells would prefer to confine themselves in the cloud layer but this, of course, would cut off the important water vapor source at the surface.

Although marine stratocumulus convection has not attracted the attention of other more violent weather systems, it appears to play an important and interesting role in the global atmospheric circulation. Like nonprecipitating trade cumulus convection, stratocumulus convection condenses water at lower levels, transports it upward and evaporates it at higher levels, and in so doing, moistens the air in the downward branches of the Hadley cell. Thus, stratocumulus and trade cumulus can be thought of as the giant humidifiers of the air flowing toward the intertropical convergence zone.

Air flowing toward the ITCZ moves through regions of varying sea surface temperature and varying large-scale divergence, and we might then question whether a horizontally homogeneous steady-state situation is ever reached. This question is investigated in Part II.

REFERENCES

Arakawa, A., 1975: Modeling clouds and cloud processes for use in climate models. Report of the international study conference on the physical basis of climate modeling, Stockholm, 29 July–10 August 1974, GARP Publ. Ser. No. 16.

Árnason, G., R. S. Greenfield and E. A. Newburg, 1968: A numerical experiment in dry and moist convection including the rain stage. *J. Atmos. Sci.*, **25**, 404–415.

Cox, S. K., 1973: Infrared heating calculations with a water vapor pressure broadened continuum. *Quart. J. Roy. Meteor. Soc.*, **99**, 669–679.

Deardorff, J. W., 1976: On the entrainment rate of a stratocumulus-topped mixed layer in a strong inversion. *Quart. J. Roy. Meteor. Soc.*, **102**, 563–582.

Flohn, H., M. Hantel and E. Ruprecht, 1968: Air-mass dynamics or subsidence processes in the Arabian Sea summer monsoon? *J. Atmos. Sci.*, **25**, 527–529.

Gunther, E. B., 1977: Eastern North Pacific tropical cyclones of 1976. *Mon. Wea. Rev.*, **105**, 508–522.

Kahn, P. H., and J. A. Businger, 1979: The effect of radiative flux divergence on entrainment of a saturated convective boundary layer. *Quart. J. Roy. Meteor. Soc.*, **105**, 303–306.

Kraus, H., and E. Schaller, 1978a: Steady-state characteristics of inversions capping a well-mixed PBL. *Bound-Layer Meteor.*, **14**, 83–104.

——, 1978b: A note on the closure in Lilly-type inversion models. *Tellus*, **30**, 284–288.

LaViolette, P. E., 1974: A satellite-aircraft thermal study of the upwelled waters off Spanish Sahara. *J. Phys. Oceanogr.*, **4**, 676–684.

Leetmaa, A., 1972: The response of the Somali Current to the southwest monsoon of 1970. *Deep-Sea Res.*, **19**, 319–325.

Lenschow, D. H., 1973: Two examples of planetary boundary layer modification over the Great Lakes. *J. Atmos. Sci.*, **30**, 568–581.

——, and E. M. Agee, 1976: Preliminary results from the Air

Mass Transformation Experiment (AMTEX). *Bull. Amer. Meteor.*, **57**, 1346–1355.

Lilly, D. K., 1968: Models of cloud-topped mixed layers under a strong inversion. *Quart. J. Roy. Meteor. Soc.*, **94**, 292–309.

——, and W. H. Schubert, 1979: The effects of radiative cooling in a cloud-topped mixed layer. Submitted to *J. Atmos. Sci.*

Ninomiya, K., 1975: Large-scale aspects of air mass transformation over the East China Sea during AMTEX '74. *J. Meteor. Soc. Japan*, **53**, 285–303.

Nitta, T., 1976: Large-scale heat and moisture budgets during the Air Mass Transformation Experiment. *J. Meteor. Soc. Japan*, **54**, 1–14.

Ogura, Y., and N. A. Phillips, 1962: Scale analysis of deep and shallow convection in the atmosphere. *J. Atmos. Sci.*, **19**, 173–179.

Paltridge, G. W., 1974: Infrared emissivity, shortwave albedo and the microphysics of stratiform water clouds. *J. Geophys. Res.*, **79**, 4053–4058.

Platt, C. M. R., 1976: Infrared absorption and liquid water content in stratocumulus clouds. *Quart. J. Roy. Meteor. Soc.*, **102**, 553–561.

Ramage, C. S., 1966: The summer atmospheric circulation over the Arabian Sea. *J. Atmos. Sci.*, **23**, 144–150.

Randall, D., 1976: The interaction of the planetary boundary layer with large-scale circulations. Ph.D. dissertation, University of California at Los Angeles, 247 pp.

——, 1979a: Conditional instability of the first kind, upside-down. Submitted to *J. Atmos. Sci.*

——, 1979b: Entrainment into a stratocumulus layer with distributed radiative cooling. Submitted to *J. Atmos. Sci.*

Schubert, W. H., 1976: Experiments will Lilly's cloud-topped mixed layer model. *J. Atmos. Sci.*, **33**, 436–446.

——, J. S. Wakefield, E. J. Steiner and S. K. Cox, 1979: Marine stratocumulus convection, Part II: Horizontally inhomogeneous solutions. *J. Atmos. Sci.*, **36**, 1308–1324.

Trewartha, G. T., 1961: *The Earth's Problem Climates*. University of Wisconsin Press, 344 pp.

U. S. Dept. of Commerce, Weather Bureau, 1959: *World Weather Records, 1941–1950*. Gov. Printing Office, Washington, DC.

U. S. Dept. of Commerce, Environmental Science Services Administration, Environmental Data Service, 1968: *World Weather Records, 1951–60*. Govt. Printing Office, Washington, DC.

U. S. Dept. of Commerce, Environmental Science Services Administration, Environmental Data Service, 1967–70: *Climatological Data, National Summary*. Govt. Printing Office, Washington, DC.

Wakefield, J. S., and W. H. Schubert, 1976: Design and execution of the marine stratocumulus experiment. Atmos. Sci. Pap. No. 256, Colorado State University, 74 pp.

Warren, B., H. Stommel and J. C. Swallow, 1966: Water masses and patterns of flow in the Somali Basin during the southwest monsoon of 1964. *Deep-Sea Res.*, **13**, 825–860.